The formation of paranodal spirals at the ends of CNS myelin sheaths requires the planar polarity protein Vangl2

Citation for published version:
Jarjour, A, Velichkova, A, Boyd, A, Lord, KM, Torsney, C, Henderson, DJ & Ffrench-Constant, C 2020, 'The formation of paranodal spirals at the ends of CNS myelin sheaths requires the planar polarity protein Vangl2', *Glia*, vol. 68, no. 9, pp. 1840-1858. https://doi.org/10.1002/glia.23809

Digital Object Identifier (DOI):
10.1002/glia.23809

Link:
Link to publication record in Edinburgh Research Explorer

Document Version:
Peer reviewed version

Published In:
Glia

The formation of paranodal spirals at the ends of CNS myelin sheaths requires the planar polarity protein Vangl2

Journal:	*GLIA*
Manuscript ID	GLIA-00391-2019.R1
Wiley - Manuscript type:	Original Research Article
Date Submitted by the Author:	n/a
Complete List of Authors:	Jarjour, Andrew; The University of Edinburgh, MRC Centre for Regenerative Medicine and MS Society/University of Edinburgh Centre for Translational Research, Scottish Centre for Regenerative Medicine; Discovery Research MRL UK, MSD, Cell Biology Velichkova, Atanaska; The University of Edinburgh, Centre for Discovery Brain Sciences Boyd, Amanda; The University of Edinburgh, MRC Centre for Regenerative Medicine and MS Society/University of Edinburgh Centre for Translational Research, Scottish Centre for Regenerative Medicine Lord, Kathryn; The University of Edinburgh, MRC Centre for Regenerative Medicine and MS Society/University of Edinburgh Centre for Translational Research, Scottish Centre for Regenerative Medicine Torsney, Carole; The University of Edinburgh, Centre for DIscovery Brain Sciences Henderson, Deborah; Newcastle University, Institute of Genetic Medicine ffrench-Constant, Charles; The University of Edinburgh, MRC Centre for Regenerative Medicine and MS Society/University of Edinburgh Centre for Translational Research, Scottish Centre for Regenerative Medicine
Topics:	Oligodendrocytes, CNS myelin, Cytoskeletal proteins, Metabolic interactions with neurons
Techniques:	Histological techniques, Electron microscopy/immunoelectron microscopy, Cellular and Developmental Neuroscience, Deletion of genes (knockout techniques), Extracellular recording techniques
Key Words:	Node of Raniver, Paranode, Cell polarity, Vangl2, Myelin

The formation of paranodal spirals at the ends of CNS myelin sheaths requires the planar polarity protein Vangl2

Abbreviated title: Vangl2 regulates CNS paranode formation

Andrew A. Jarjour*[1§], Atanaska N. Velichkova[2], Amanda Boyd[1], Kathryn M. Lord[1], Carole Torsney[2], Deborah J. Henderson[3], Charles ffrench-Constant[1]

[1] *MRC Centre for Regenerative Medicine and MS Society/University of Edinburgh Centre for Translational Research, Scottish Centre for Regenerative Medicine, The University of Edinburgh, 5 Little France Drive, Edinburgh, EH16 4UU, UK*

[2] *Centre for Discovery Brain Sciences, The University of Edinburgh, Hugh Robson Building, 15 George Square, Edinburgh, EH8 9XD, UK*

[3] *Institute of Genetic Medicine, Newcastle University, Centre for Life, Central Parkway, Newcastle upon Tyne, NE1 3BZ, UK.*

[§] *Current address: MSD UK Discovery Centre MRL, London Bioscience Innovation Centre, 2 Royal College Street, London, NW1 0NH, UK.*

*andrew.jarjour@merck.com

ACKNOWLEDGMENTS

We thank David Lyons and Anna Williams for their helpful comments about the manuscript, and Bertrand Vernay for his assistance with image analysis. All authors reviewed and commented on the paper before submission. Funding for this project was provided by the Wellcome Trust and the UK Multiple Sclerosis Society.

CONFLICT OF INTEREST STATEMEMT

The authors declare no competing interests.

WORD COUNT

Total: 12012 ; Abstract: 200 ; Introduction: 953 ; Materials and Methods: 2024 ; Results: 2291 ; Discussion: 2275.

ABSTRACT

During axonal ensheathment, non-compact myelin channels formed at lateral edges of the myelinating process become arranged into tight paranodal spirals that resemble loops when cut in cross section. These adhere to the axon, concentrating voltage-dependent sodium channels at nodes of Ranvier and patterning the surrounding axon into distinct molecular domains. The signals responsible for forming and maintaining the complex structure of paranodal myelin are poorly understood. Here, we test the hypothesis that the planar cell polarity determinant Vangl2 organizes paranodal myelin. We show that Vangl2 is concentrated at paranodes and that, following conditional knockout of Vangl2 in oligodendrocytes, the paranodal spiral loosens, accompanied by disruption to the microtubule cytoskeleton and mislocalization of autotypic adhesion molecules between loops within the spiral. Adhesion of the spiral to the axon is unaffected. This results in disruptions to axonal patterning at nodes of Ranvier, paranodal axon diameter and conduction velocity. When taken together with our previous work showing that loss of the apico-basal polarity protein Scribble has the opposite phenotype – loss of axonal adhesion but no effect on loop-loop autotypic adhesion – our results identify a novel mechanism by which polarity proteins control the shape of nodes of Ranvier and regulate conduction in the CNS.

KEYWORDS:
Oligodendrocyte, myelin, paranode, cell polarity, Vangl2, node of Ranvier

MAIN POINTS:

The architecture of the paranodal loops that border myelin sheaths enables rapid conduction by patterning ensheathed axons. Jarjour et al. show that the planar polarity protein Vangl2 maintains the intracellular adhesion that holds these loops together.

INTRODUCTION

Myelination in the CNS provides electrical insulation along the length of the sheath and enables rapid conduction by restricting the voltage-dependent sodium channels responsible for propagating action potentials to the small gaps between adjacent sheaths - the nodes of Ranvier. Together, these ensure that the action potential ‘jumps’ from node to node, so generating rapid and energy efficient saltatory conduction (Huxley & Stampfli, 1949; Tasaki & Takeuchi, 1942). Myelin also provides metabolic support by enabling the transport of substrates for ATP generation by the citric acid cycle into the ensheathed axon (Fünfschilling et al., 2012). While tight apposition of myelin lamellae is essential for the proper functioning of the sheath (Boison, Bussow, Durso, Muller, & Stoffel, 1995), the non-compacted regions of the myelin sheath also play a critical role in regulating conduction along, and providing metabolic support to, the axon. Non-compact myelin consists of specialized channels that are formed as the myelin sheath is compacted and oligodendroglial cytoplasm is extruded to the edges of myelinating processes (Fig. 1A). Whilst the cytoplasm-filled channels formed once wrapping and compaction is complete are continuous within the sheath, they are subdivided into functionally and molecularly distinct regions (reviewed byreviewed byreviewed byreviewed byreviewed byreviewed byreviewed byreviewed bySimons, Snaidero, & Aggarwal, 2012). The channel at the leading edge of the myelinating process forms the adaxonal inner tongue that runs along the surface of the axon under the sheath. Here adaxonal myelin proteins including the transporter MCT1 and CNPase are required for long-term metabolic support of the axon (Lappe-Siefke et al., 2003; Lee et al., 2012). By contrast, the paranodal channels, so named because of their location abutting the node of Ranvier, are formed at the lateral edges of the myelinating process and form a tight spiral. When cut in cross section along the axon, the turns of the spiral give the appearance of a series of loops – the so-called paranodal loops (Fig. 1B). This paranodal spiral forms a close association with the underlying axon through an adhesion complex comprising the 155 kDa isoform of neurofascin (NFC155) on the oligodendrocyte binding to contactin-1 and Caspr on the axon (Charles et al., 2002; Rios et al., 2000). The resulting tight axo-glial adhesion at the paranodal domain acts as a physical and electrical barrier separating the voltage-gated sodium channels required for saltatory conduction from the delayed rectifier potassium channels at the juxtaparanode (reviewed by reviewed by reviewed by reviewed by reviewed by reviewed by reviewed by reviewed by Zollinger, Baalman, & Rasband, 2015). Another distinct set of adhesion proteins hold adjacent turns of the spiral together (so maintaining a tight spiral), including the tight junction protein Claudin-11 and gap junction protein Connexin-32 (Cx32), which are both essential for normal conduction in the CNS (Fig. 1B, Devaux & Gow, 2008; Sargiannidou et al., 2009). These adhesion molecules are confined to lateral membranes of the channel, where they form autotypic junctions between neighbouring paranodal loops (Gow et al., 1999; Kamasawa et al., 2005). While therefore essential for the complex three-dimensional organization and stability of the myelin sheath, the mechanisms responsible for the precise localization of the distinct sets of adhesion proteins within the paranodal channel and its resultant polarization (Fig. 1C, arrow) are unknown.

The precise arrangement of axo-glial and autotypic adhesions within the paranodal channel represents a remarkable example of sub-cellular polarization. In other cell types, the localization of proteins to specific membrane subdomains is controlled by evolutionarily-conserved regulators of cell polarity. In epithelial cells, where the function of polarity proteins is best understood, this occurs along two perpendicular axes: Apico-basal polarity (ABP) signalling controls the distribution of proteins between the inner and outer faces of the epithelium, while the planar cell polarity (PCP) pathway operates in an orthogonal plane to the ABP pathway, conferring an ‘anterior’ and ‘posterior’ identity to lateral membranes within epithelial cells, and a directionality to the epithelium itself (reviewed by reviewed by reviewed by reviewed by reviewed by reviewed by reviewed by reviewed by Campanale, Sun, & Montell, 2017). We have previously demonstrated that Scribble, a key regulator of ABP in epithelia (Bilder & Perrimon, 2000), is required for paranodal axo-glial adhesion, as revealed by the detachment of loops from the axon following the conditional elimination of Scribble expression in oligodendroglia (Fig 1D,E,Jarjour et al., 2015). However, very little is known about the role played by the other major polarity signalling pathway, PCP, in CNS myelination. Among the highly evolutionarily-conserved core PCP proteins, the four-pass transmembrane protein Van Gogh-like 2 (Vangl2), a vertebrate orthologue of *Drosophila* Van Gogh/Strabismus, is of particular interest owing to its close physical and functional interaction with Scribble (Courbard, Djiane, Wu, & Mlodzik, 2009; Montcouquiol et al., 2003; Yates et al., 2013). In neurons, Vangl2 has been implicated in the regulation of neurite outgrowth (Dos-Santos Carvalho et al., 2020), axon guidance (Leung et al., 2016; Sun, Purdy, & Walsh, 2016), dendritic spine morphology (Okerlund, Stanley, & Cheyette, 2016) and glutamatergic synapse formation (Thakar et al., 2017). It has previously been reported that the Vangl2 binding protein Prickle1 is expressed by oligodendroglia (Liu et al., 2013) and promotes their differentiation (Zilkha-Falb, Gurevich, Hanael, & Achiron, 2017), but the role played by Vangl2 itself in paranode formation and other oligodendroglial functions is unknown. Here, we have addressed this question by removing Vangl2 from oligodendrocytes. We reveal a striking phenotype in which the paranodal spiral loosens and unwinds and demonstrate that, as in epithelia, Vangl2 regulates the precise localization of junctional adhesion proteins. Within the paranodal spiral these adhesion proteins normally stabilize the paranodal channel in a tight spiral around the axon, a spiral that patterns the underlying axon. Thus, we reveal a novel role for PCP signalling molecules in both shaping and patterning the paranodal axon.

MATERIALS AND METHODS

CONTACT FOR REAGENT AND RESOURCE SHARING

Requests for further information, resources, and/or reagents should be addressed to Andrew Jarjour (andrew.jarjour@merck.com).

REAGENTS USED

REAGENT or RESOURCE	SOURCE	IDENTIFIER
Antibodies		
Mouse anti-pan Na$_V$	Sigma-Aldrich	Cat# S8809; RRID: AB_477552
Rabbit anti-Vangl2	Abcam	Cat# ab76174; RRID: AB_1925553
Mouse anti-Caspr	Antibodies Inc.	Cat# 75-001; RRID: AB_2083496
Rabbit anti-Caspr	Abcam	Cat# ab34151; RRID: AB_869934
Chicken anti-NFH	BioLegend	Cat# 822601; RRID: AB_2564859
Rabbit anti-K$_V$1.1	Abcam	Cat# ab32433; RRID: AB_2265066
Rabbit anti-Claudin-11	Thermo Fisher	Cat# 36-4500; RRID: AB_2533259
Mouse anti-Connexin-32 (IgG2a)	Thermo Fisher	Cat# 35-8900; RRID: AB_87604
Rabbit anti-Septin-8	Proteintech	Cat# 11769-1-AP; RRID: AB_2185006
Mouse anti-βIV Spectrin (IgG2b)	Antibodies Inc.	Cat# 75-377; RRID: AB_2315818
Mouse anti-βII Spectrin (IgG1)	BD Biosciences	Cat# 612563; RRID: AB_399854
Goat anti-MAG	Santa Cruz	Cat# sc-9544; RRID: AB_670102
Rat anti-MBP	AbD Serotec	Cat# MCA409S; RRID: AB_325004
Goat anti-Vangl2	Abcam	Cat# ab60172; RRID: AB_946101
Rabbit anti-Prickle1	Proteintech	Cat# 22589-1-AP; RRID: N/A
Donkey anti-mouse IgG – Alexa Fluor 568	Thermo Fisher	Cat# A10037; RRID: AB_2534013
Donkey anti-rabbit IgG – Alexa Fluor 488	Thermo Fisher	Cat# A21206; RRID: AB_141708
Donkey anti-goat IgG – Alexa Fluor 647	Thermo Fisher	Cat# A21447; RRID: AB_141844
Donkey anti-chicken IgY – DyLight 405	Jackson Imm.	Cat# 703-475-155; RRID: AB_2340373
Goat anti-mouse IgG2a – Alexa Fluor 488	Thermo Fisher	Cat# A21131; RRID: AB_141618
Goat anti-rabbit IgG – Alexa Fluor 488	Thermo Fisher	Cat# A11008; RRID: AB_143165
Goat anti-mouse IgG1 – Alexa Fluor 633	Thermo Fisher	Cat# A21126; RRID: AB_1500804
Goat anti-mouse IgG2b – Alexa Fluor 568	Thermo Fisher	Cat# A21144; RRID: AB_1500898
Donkey anti-rat IgG – Alexa Fluor 568	Abcam	Cat# ab175475; RRID: AB_2636887
Donkey anti-goat – Alexa Fluor 488	Thermo Fisher	Cat# A11055; RRID: AB_142672
Goat anti-CD140a (PDGFαR)	Biolegend	Cat#135902; RRID: AB_1953328
Anti-Griffonia Simplicifolia Lectin	Vector Labs	Cat# L-1100; RRID: AB_2336491
Bacterial and Virus Strains		
N/A		
Chemicals, Peptides, and Recombinant Proteins		
Formaldehyde, 37% solution	Sigma-Aldrich	Cat# 252549
Glutaraldehyde, 25% solution	TAAB Laboratories	Cat# G011/2
Propylene oxide	Thermo Fisher	Cat# 10286460
Taab 812 Premix Kit-Medium	TAAB Laboratories	Cat# T031
N-acetyl cysteine	Sigma-Aldrich	Cat# A9165
B27 supplement	Thermo Fisher	Cat# 17504-044
Biotin	Sigma-Aldrich	Cat# B4639
Trace elements B	Thermo Fisher	Cat# MT99175CI

Insulin, human recombinant	Simga-Aldrich	Cat# 91077C
Pen-strep-glu	Thermo Fisher	Cat# 10378
DMEM high glucose with Glutamax	Thermo Fisher	Cat# 31966-021
Sodium selenite	Sigma-Aldrich	Cat# S5261
Putrescine	Sigma-Aldrich	Cat# P5780
Forskolin	Sigma-Aldrich	Cat# F6886
Progesterone	Sigma-Aldrich	Cat#P8783
Apo-transferrin	Sigma-Aldrich	Cat# T1147
Bovine serum albumin	Sigma-Aldrich	Cat# A8806
Recombinant PDGF-AA	Peprotech	Cat# 100-13A;
Recombinant NT3	Peprotech	Cat# 450-03
Recombinant CNTF	Peprotech	Cat# 450-13
Poly-L-lysine	Sigma-Aldrich	Cat# P6282
Critical Commercial Assays		
gentleMACS dissociator	Miltenyi Biotec	130-093-235
Neural Tissue Dissociation Kit (P)	Miltenyi Biotec	130-092-628
C tubes	Miltenyi Biotec	130-093-237
Experimental Models: Organisms/Strains		
Mouse: CNP$^{tm1(cre)Kan}$	(Lappe-Siefke et al., 2003)	RRID: MGI: 3051754
Mouse: Vangl2 flox	(Ramsbottom et al., 2014)	N/A
Other		
Acupuncture needles, 25 mm long, 0.25 mm diameter	Journal of Chinese Medicine	Cat# NA3210
SuperFrost Plus slides	Thermo Fisher	Cat# 10149870

EXPERIMENTAL MODEL AND SUBJECT DETAILS

Mice in which the *Vangl2* gene was targeted for condition elimination by insertion of LoxP sites flanking exon 4 (Ramsbottom et al., 2014) were crossed with mice expressing Cre recombinase under the control of the *2'-3' cyclic nucleotide phosphodiesterase* (CNP) gene (Lappe-Siefke et al., 2003) to generate *CNP*$^{+/Cre}$*:Vangl2*$^{fl/fl}$ mice, in which *Vangl2* expression is conditionally eliminated in myelinating glia. Both male and female mice (1-8 weeks of age) were used. A total of 110 mice were used for all studies described in this study. All animal work conformed to UK legislation (Scientific Procedures) Act 1986 and to the University of Edinburgh regulations.

METHOD DETAILS

Mouse oligodendroglial cultures

8 postnatal day 7 mouse pups were killed by injection with a 1:1 mix of Dormitor and Vetelar and their cortices removed. Cortices were dissociated using a gentleMACS dissociator using C tubes with the Neural Tissue Dissociation Kit (Miltenyi Biotec). Cell suspensions were subjected to immunopanning, first by negative selection using 'bacterial' (untreated) culture plates coated with anti-Griffonia Simplicifolia Lectin, then by positive selection using antibodies against platelet-derived growth factor receptor α (PDGFRα). Positively-selected cells were cultured on PDL-coated T-75 flasks in OPC-Sato medium (high-glucose DMEM with, 1% apo-Transferrin, 1% bovine serum albumin, 9.934 mM Putrescine dihydrochloride, 19.88 μM progesterone, 0.2313 μM sodium selenite, B27 supplement, 0.3678 mM N-acetyl cysteine, 5 μg/ml insulin, Trace Element B mix, 4.093 nM biotin and 5 nM forskolin) with 10 ng/ml PDGF-AA and 5 ng/ml neurotrophin 3 (NT3) at 37°C in 7.5% CO_2. 50% medium changes were carried out every day for 7 days to allow OPCs to proliferate. When OPCs reached confluence, cells were seeded on PDL-coated 22 mm glass coverslips, and differentiated into oligodendrocytes in OPC-Sato medium with 5 ng/ml NT3 and 10 ng/ml ciliary neurotrophic factor (CNTF) for at 37°C in 7.5% CO_2 for 2 days. For immunocytochemical analyses, cultures were fixed with 4% paraformaldehyde and washed twice in PBS, and blocked with blocking solution (4% heat-inactivated donkey serum, 2% BSA, and 0.1% Triton X-100 in PBS). Cultures were incubated overnight in primary antibodies diluted in blocking solution. Following repeated washes with PBS, cultures were incubated with secondary antibodies, washed with PBS, and then mounted. Confocal z-stacks were acquired using Leica SP8 inverted confocal microscope (63x objective, zoom 2). Images were processed using ImageJ and Photoshop (Adobe, USA) software.

Teased spinal cord fibres

34 postnatal day 14 or 60 mice were fixed by cardiac perfusion with 4% formaldehyde in PBS. The cervical spinal cord was dissected out, and postfixed for 30 minutes in cold 4% formaldehyde in PBS before being stored in PBS at 4ºC for at most 48 hours. The meninges were removed, and the ventral white matter isolated into cold PBS, and cut into pieces roughly 2 mm long. Fibres were then teased onto SuperFrost Plus slides (for standard confocal imaging) or TESPA-coated coverslips (for gSTED super-resolution imaging) using acupuncture needles. Slides were stored at -20 ºC in airtight containers until immunolabelling. Immunohistochemical labelling was carried out as described above for cultures. For standard confocal imaging, z-stacks were acquired using Leica SP8 inverted confocal microscope (63x objective, 1.40 N.A.). Maximum intensity projection images of Z-stacks were used for analysis. Images were processed using ImageJ and Photoshop (Adobe, USA) software. For immunolabelling of STED images, the secondary antibodies used were Atto647N-conjugated goat anti-rabbit IgG for Claudin-11 immunolabelling and Alexa 568-conjugated goat anti-mouse IgG (H+L) for Caspr labelling. For STED images, z-stacks were acquired using a Leica TCS SP8 STED 3x microscope (100x objective, 1.40 N.A.), using the 775 nm laser for depletion. Stacks were deconvolved using the Huygens STED deconvolution package (Scientific Volume Imaging B.L., Netherlands) integrated in Leica LAS AF software prior to analysis.

Transmission electron microscopy

42 postnatal day 14 or 60 mice were fixed by cardiac perfusion with 4% formaldehyde/2.5% glutaraldehyde in 0.1 M phosphate buffer, pH 7.3. Samples were postfixed in 4% formaldehyde/2.5% glutaraldehyde in 0.1 M phosphate buffer, pH 7.3, for 2 hours, then in 1% glutaraldehyde in 0.1M phosphate buffer for 14 days, washed in PBS and post-fixed in 1%

Osmium Tetroxide in 0.1M phosphate buffer for 60 minutes. The samples were then dehydrated in increasing concentrations of ethanol and embedded in epoxy resin. Sections, 1µm thick, were cut on a Reichert OMU4 ultramicrotome (Leica Microsystems), stained with Toluidine Blue and viewed in a light microscope to select suitable areas for investigation. 60nm ultrathin sections were cut from selected areas, stained in Uranyl Acetate and Lead Citrate and then viewed using a JEOL JEM-1400 Plus transmission electron microscope. Images were acquired using a Gatan OneView camera (Gatan).

Recording of compound action potentials

Following decapitation under isoflurane anaesthesia, optic nerves from a total of 26 postnatal day 60 mice were dissected free into oxygenated ice-cold dissection solution. The nerves were incubated for 1h in 36–37°C oxygenated recovery solution prior to transfer to a recording chamber continuously perfused with oxygenated Krebs' solution (1–2 mL/min) at room temperature. The oxygenated Krebs' solution contained (in mM) 125 NaCl, 2.5 KCl, 1.25 NaH_2PO_4, 26 $NaHCO_3$, 25 glucose, 1 $MgCl_2$, and 2 $CaCl_2$, pH 7.4. The recovery solution was identical to Krebs' solution apart from 1.5 $CaCl_2$ and 6 $MgCl_2$. Dissection solution was the same as the recovery solution with added 1 mM kynurenic acid.

Two glass suction electrodes were used to record compound action potentials, one for electrical stimulation and the second for recording compound action potentials (CAPs). The optic nerves were stimulated 3x at 0.2 Hz (0.1 ms duration) with an ISO-flex stimulus isolator (A.M.P.I Intracel). The applied stimulation intensities were 1, 2.5, 5, 7.5, 10-50 (in steps of 5 µA), 60-100 (in steps of 10 µA), and 125–500 µA (in steps of 25 µA). The CAPs are composed of three main components that could be differentiated on the basis of activation threshold and conduction velocity, each displaying a characteristic triphasic (positive-negative-positive) responses that overlap (Fig 5A). Data were acquired and recorded using a Cygnus ER-1 differential amplifier (Cygnus Technologies Inc.) and pClamp 10 software (Molecular Devices). Data were filtered at 10kHz and sampled at 50kHz.

QUANTIFICATION AND STATISTICAL ANALYSES

All confocal and TEM images were analysed using FiJi software (Schindelin et al., 2012). For analysis of separation between paranodal loops, neighbouring loops were considered separated if they were clearly separated by more than one membrane width for at least one-third of the length of the border between the loops. For analysis of detachment of paranodal loops from the axon, a loop was considered detached if a separation of at least 100 nm was measured between the loop and axon. G-ratio was determined by dividing axon diameter by the total diameter of the axon and overlying myelin sheath. Axon diameter was calculated from measured axon perimeter based on an assumption of circularity. For measurements taken from optic nerve, the diameter of the myelinated axon was determined similarly. For measurements of g-ratio in spinal cord, where myelin sheaths often appeared uncompacted, myelin sheath thickness was measured directly at the point at which the myelin sheath was most compact, and myelinated axon diameter was determined by adding this value to the calculated axon diameter. Internodal axonal diameter was measured at the location in the field where the internodal axon was thickest. Paranodal axonal diameter was measured at the innermost border of whichever second loop from the inside is located closer to the node (where inner means towards the internode).

For analyses of trailing paranodal domains, a paranode was scored as trailing if either four or more turns of Caspr spiral or a 2 µm or longer continuous region of Caspr immunolabelling separated from the paranodal Caspr domain were visible within 20 µm from the juxtaparanodal end of the continuous paranodal Caspr immunopositive domain. For analyses of the separation between axonal domain markers at nodal regions, the shortest distance along the axon between the edge of one domain and the other was measured. When these domains contacted each other or overlapped, the distance was measured as 0. For measurements of the width of axonal domains, the distance measured was the maximal distance along the axon where continuous immunoreactivity could be observed.

For gSTED analysis of immunofluorescence intensity of Claudin-11 or Caspr labelling, image stacks were cropped to eliminate half the paranodal spiral so that ‘top’ and ‘bottom’ edges of each turn of the spiral were not double-counted and a maximum intensity projection was performed. On the projected image, a 2 pixel-wide line was drawn longitudinally across the paranodal spiral starting at the nodal end and an intensity plot was generated. Maxima and minima were identified using the BAR Scripts 1.5.1 ‘Find Peaks’ macro (Ferreira T, 2017).

Clampfit 10.7.0.3 was used for analysing the CAP recordings. The activation threshold for each component was defined as the lowest stimulation intensity at which the negative component of the triphasic response was clearly identifiable. The conduction velocity was calculated based on the latency to the negative peak of each component at 100 μA. Group comparisons were made using two-way ANOVA followed by Sidak’s multiple comparisons test.

Statistical analyses were performed using GraphPad Prism. Descriptions of statistical analyses performed are provided in the figure legends. All data are presented as mean ± standard error of the mean (SEM).

DATA AVAILABILITY STATEMENT

The data that support the findings of this study are available from the corresponding author upon reasonable request.

RESULTS

Vangl2 is expressed by oligodendroglia and is localized to CNS paranodes

To ask whether Vangl2 plays a role in organising the myelin sheath, we first examined its distribution within oligodendroglia and in CNS myelin. We confirmed that Vangl2 is expressed by MBP-positive oligodendroglia. Vangl2 is localized to cell bodies and processes in wild-type oligodendrocytes but is excluded from myelin-like membrane sheets (Fig. 2A,B). It is localised predominantly to Caspr-immunolabelled paranodes in teased spinal cord preparations from postnatal day 60 (P60) spinal cord, although some internodal Vangl2 labelling was also observed (Fig. 2E,F). We observed a similar distribution of the Vangl2 binding partner Prickle1 in both cultured oligodendrocytes (Fig. S1A-C), and in P60 teased spinal cord preparations (Fig. S1D,E).

To confirm that the paranodal immunolabelling represented Vangl2 expression in oligodendrocytes, and to enable the further studies below, we conditionally eliminated Vangl2 expression from myelinating glia by creating *Vangl2* cKO ($CNP^{+/Cre}:Vangl2^{fl/fl}$) mice. Conditional elimination of Vangl2 in these oligodendroglia was verified in purified cultures derived from Vangl2 cKO cortex (Fig. 2C,D), where Vangl2 immunolabelling was substantially decreased relative to that observed in Vangl2 WT ($CNP^{+/+}:Vangl2^{fl/fl}$) oligodendroglia (Fig. 2A,B). Importantly, immunolabelling of teased axons from the mice showed that paranodal Vangl2 was absent from Vangl2 cKO paranodes (Fig. 2G,H) relative to Vangl2 WT paranodes (Fig. 2E,F), confirming that the Vangl2 present at CNS paranodes is expressed by oligodendrocytes and not by the underlying axon.

Oligodendroglial Vangl2 organizes CNS paranodes and nodes of Ranvier

Our previous findings demonstrated that the apico-basal polarity protein Scribble is required for normal CNS myelin initiation, thickness and paranodal axo-glial adhesion (Jarjour et al., 2015). By contrast, Vangl2 cKO animals had no reduction in the proportion of myelinated axons in P14 optic nerve (Fig. S2A-D) nor any change in g-ratio in P60 spinal cord (Fig. S2E-H), suggesting that Vangl2 does not regulate myelin sheath formation or wrapping in the CNS. To assess paranodal architecture, we examined the distribution of the axonal molecule Caspr, part of the axoglial adhesion complex that marks sites of axon-loop contact. Normally, the tight apposition of paranodal loops to one another means that, using immunofluorescent light microscopy, the Caspr spiral appears as a uniform band, as was observed in P60 teased fibre preparations from Vangl2 WT spinal cord (Fig 3A,C). In the Vangl2 cKO, however, paranodal organization was disrupted as evidenced by the loosening of the Caspr spiral. An increased proportion of Vangl2 cKO paranodes display loops that extend back within the internode as a loose spiral (Fig. 3B,D, quantification in E). In some cases, the interruption between paranodal loops was observed as a split between the loops closest to the node and those trailing back into the internode (Fig.3F, arrows). In contrast to our observations in CNS myelin lacking Scribble, we did not observe a significant increase in disengagement of paranodal loops from the axonal surface in Vangl2 cKO spinal cord at P60 using transmission electron microscopy (TEM, Fig. 3H). However these TEM studies did show that, even when no obvious differences in the 'tightness' of the paranodal spiral in regions closest to the node could be observed in Vangl2 cKO teased fibres using standard confocal imaging, a significantly increased proportion of neighbouring paranodal loops were separated (Fig. 3G,I (arrowheads), J).

To ask whether this loosening of the paranodal spiral seen at P60 reflects a failure of the formation of the paranodal structure or a loss of its maintenance once formed, we analysed P14 spinal cord – a time when axons are still growing in length. Here we found using EM that slight separations between loops could be seen even at this early time point (Figure S3), although statistical significance was not reached until the axons lengthened at P60. We conclude, therefore, that Vangl2 is required for normal adhesion between paranodal loops in the CNS, with the consequent phenotype of a loosened spiral fully revealed once the axon has lengthened. Vangl2 is not, however, required for the adhesion between loops and axon.

To further quantify the spacing between turns of the paranodal spiral, paranodal Caspr immunolabelling was imaged using super-resolution gated STED (gSTED) confocal microscopy. The distance between turns of the Caspr spiral, measured by determining the distance between Caspr intensity peaks, was increased at Vangl2 cKO paranodes (Fig. 3M) relative to wild-type paranodes (Fig. 3K, quantified in L). Increased spacing between loops became more pronounced with distance from the node of Ranvier, as visualised by the increase in slope of the best-fit line when plotting distance between turns against distance from the node of Ranvier (Fig. 3N).

Vangl2 organizes the CNS myelin sheath and patterns the underlying axon

Two of the key functions of CNS paranodal axo-glial adhesions are to promote the concentration of an axolemmal protein complex containing voltage-gated sodium (Na_V) channels at nodes of Ranvier (Zonta et al., 2008), and to form a barrier that separates the nodal complex from a juxtaparanodal complex containing voltage-gated potassium (Kv) channels(Bhat et al., 2001). To determine whether paranodal function was disrupted in the absence of Vangl2 expression by oligodendroglia, we examined axonal organization in teased spinal cord preparations from P60 *Vangl2* cKO mice. We observed that, while Caspr-immunolabelled paranodes flank Na_V-immunopositive nodes of Ranvier in wild-type CNS (Fig. 4A,C,E), paranodal Caspr extends into the nodes of Ranvier of the *Vangl2* cKO mice, narrowing the nodal 'gap' between neighbouring paranodes (Fig. 4B (arrow), F, G), and also in towards the internode (Fig. 4B, arrowhead). Reduced distance across the node of Ranvier could also be detected by TEM in P60 spinal cord (Fig. S4). Surprisingly, despite the narrowing of the node of Ranvier in the Vangl2 cKO CNS, the nodal Na_V immunolabelled domain was widened, with Na_V labelling extending laterally into the paranodes (Fig. 4D (arrowheads), F, H) with no significant difference in the mean intensity of nodal Na_V immunofluorescence observed in Vangl2 cKO teased spinal cord at P60 (Fig. 4I). This widening of the Na_V-labelled domain in Vangl2 cKOs was observed in all rather than a subset of nodes, and was not dependent on axon diameter (data not shown).

We also observed a similar change when we examined the distribution of axonal spectrins at Vangl2 cKO nodes of Ranvier. The mutual exclusion of the βIV spectrin-containing nodal cytoskeleton (Fig. S5A,E) and the βII spectrin-containing complex underlying the paranodal cytoskeleton (Fig. S5C,E) is a key mediator of the paranode's Na_V clustering and barrier functions(Amor et al., 2017). We observed that in Vangl2 cKO CNS, the width of nodal βIV spectrin domains were widened (Fig. S5B,F,H), while the distance across the nodal gap in βII spectrin labelling was decreased (Fig. S5D,F,G), mirroring the changes in Caspr and Na_V distribution observed in these animals. The observation that axonal nodal and paranodal protein complexes and their underlying cytoskeleta are mislocalized in Vangl2 cKO CNS shows that oligodendroglial Vangl2 is essential to maintain the separation between axonal nodal and paranodal domains in the CNS.

Next, we investigated whether Vangl2 plays a role in regulating the border between the paranodal and juxtaparanodal domains. While we observed a clear paranodal separation between immunolabelling for juxtaparanodal $K_V1.1$ (Fig. 4J,N) and nodal Na_V (Fig. 4L,N) in wild-type CNS, the $K_V1.1$ immunopositive domain was widened in Vangl2 cKO CNS (Fig. 4K,O,P), where it invaded paranodes, reducing the distance measured between Na_V and $K_V1.1$-labelled domains (Fig. 4O (arrows), Q). These data indicate that Vangl2 is essential for maintaining the paranodal 'barrier' between the juxtaparanodal and nodal domains in the CNS. Notably, these findings diverge from our previous observation of a similar disruption of paranodal barrier function in mice lacking oligodendroglial Scribble expression(Jarjour et al., 2015) in that in the Scribble cKO mice axo-glial adhesion of the paranodal loops is disrupted, whilst the disruption of axonal patterning in Vangl2 cKO CNS occurs despite the presence of largely intact paranodal axo-glial adhesion. We can therefore conclude that polarity proteins Vangl2 and Scribble act through different mechanisms at CNS paranodes.

Finally, we examined the transition between the internodal and paranodal domain by examining the distribution of Septin-8, a component of the septin cytoskeleton that is restricted to the innermost wrap of internodal myelin (Patzig et al., 2016). In teased fibre preparations from wild-type spinal cord, we typically observed a clear separation between internodal Septin-8 and paranodal Caspr labelling (Fig. 4R,T,V), with the former restricted to the leading edge (or inner tongue) of the myelin sheath while the latter is present only in the lateral cytoplasmic channels that for the paranodal spiral. In Vangl2 cKO fibres, however, there was a significant increase in the proportion of paranodes at which Septin-8 immunolabelling invaded the paranodal domain (Fig. 4S,U,W (arrowheads), X). A closer examination using gated STED (gSTED) superresolution confocal microscopy indicated that while Septin-8 labelling was interspersed with that for Caspr in the paranodal spirals of the Vangl2 cKO fibres, their distribution did not overlap (Fig. 4X-AA). The invasion of the paranodal spirals in these mutants by an internodal non-compact myelin protein is consistent with Vangl2 also playing an important role in the functional division between internodal and paranodal non-compact myelin.

Vangl2 is required for local regulation of axon diameter at CNS paranodes

In addition to patterning the underlying axon into distinct molecular domains, the myelin sheath physically shapes the axon. Contact between oligodendrocytes and axons promotes radial axonal growth during development (Sanchez, Hassinger, Paskevich, Shine, & Nixon, 1996), with the internodal axon diameter being greater than that of the paranode and node in the adult CNS (Hildebrand & Skoglund, 1971). When the ratio of paranodal axon diameter (dP) to internodal axon diameter (dI) was measured in Vangl2 cKO spinal cord at P60, an increased dP/dI ratio relative to that observed in wild-type spinal cord (Fig. 5A,B,E) was observed. Interestingly, this difference between Vangl2 cKO and WT axons was not seen in P14 spinal cord, a stage at which axons are still increasing in diameter (Fig. 5C,D,F). We conclude that oligodendoglial Vangl2 is essential for the local regulation of axon diameter at CNS paranodes.

Increased conductivity in Vangl2 cKO CNS

The observed disruptions to axonal domain organization and the regulation of axon diameter at nodal regions in the Vangl2 cKO raised the question of how these changes, particularly to the length and diameter of the node of Ranvier, affect conduction. When compound action potentials (CAPs) were measured in the optic nerve at P60, we observed three peaks (Fig. 6A, arrowhead, black arrow, grey arrow), as has previously been reported (Foster, Connors, & Waxman, 1982). Across all three peaks, conduction velocities were increased in Vangl2 cKO nerves compared to wild-type controls (Fig. 6B). Further analysis revealed that the minimum stimulus intensity required to elicit each component of the CAP was decreased in Vangl2 cKO nerves (representative traces shown in Fig. 6C, quantification in Fig. 6D). These findings suggest that myelination by Vangl2 cKO oligodendrocytes results in increased conductivity in the CNS.

Vangl2 regulates the distribution of autotypic adhesion proteins in CNS paranodes

The observed disruption to axonal shape and patterning at nodes of Ranvier and, consequently, on conduction as a result of a 'loosened' paranodal spiral following conditional Vangl2 deletion in oligodendroglia raises the question of the mechanism by which Vangl2 'tightens' the spiral. Autotypic tight junctions containing Claudin-11 (Gow et al., 1999) and gap junctions comprised of Connexin-32 (Cx32,Kamasawa et al., 2005) have been reported to bridge loops in CNS paranodal myelin, suggesting that these complexes may be responsible for mediating adhesion between turns of the paranodal spiral. Vangl2 has previously been reported to regulate tight junction organization and claudin-1 localization in uterine luminal epithelium (Yuan et al., 2016), raising the possibility that it may function similarly to localize Claudin-11-containing tight junctions in paranodal myelin. To test this and so provide a mechanism for the loosening of the paranodal spiral in the Vangl2 cKO mice, we imaged Claudin-11 immunolabelling within the loops using super-resolution gSTED confocal microscopy. Standard confocal imaging revealed that the spiral of paranodal Claudin-11 immunolabelling was loosened and extended laterally along the axon in Vangl2 cKO teased spinal cord preparations (Fig. 7B) relative to its distribution in wild-type paranodes (Fig. 7A). When imaged using gSTED, autotypic Claudin-11-positive tight junctions in wild-type paranodes (red in Fig. 7C, white in Fig. 7E) appear as a tight spiral surrounding the spiral defined by Caspr-immunolabelled axo-glial adhesions (green in Fig. 7C, D). In Vangl2 cKO paranodes, by contrast, the Caspr-immunopositive paranodal spiral is still apparent but Claudin-11 immunolabelling appears more diffuse (Fig. 7D,F). To quantify this, paranodal intensities were measured by drawing a line through the middle of paranodes (yellow lines in Fig. 7E,F), and maximum and minimum intensity levels across each plot (shown as red and blue dots, respectively, in Fig. 7G,I) were analysed. The difference between mean intensity values at maxima and minima were decreased at Vangl2 cKO paranodes (Fig. 7H), confirming that

Claudin-11 is mislocalized away from the normal band of tight junctions linking the paranodal spiral in Vangl2 cKO CNS.

Studies in epithelial cells show a properly-organized microtubule cytoskeleton to be of critical importance to tight junction homeostasis and barrier function (Glotfelty, Zahs, Iancu, Shen, & Hecht, 2014), suggesting a key role for the paranodal microtubules in maintaining the architecture and function of the loops. As Vangl2 regulates microtubule organization and integrity in Sertoli cells of the seminiferous epithelium (Chen, Xiao, Lui, Lee, & Cheng, 2018), we investigated whether the microtubule cytoskeleton within paranodes was also affected by Vangl2 deletion. We found that fewer microtubule cross-sections could be observed in Vangl2 cKO spinal cord paranodes at P60 (Fig. 7J,L, arrowheads), resulting in a significantly decreased paranodal microtubule density (Fig. 7K). This finding is consistent with a mechanism in which the observed mislocalization of Claudin-11, which associates with microtubules through interactions with Sec8 and CASK (Anitei et al., 2006), is a consequence of a disrupted microtubule cytoskeleton in Vangl2 cKO paranodes.

DISCUSSION

Here, we report that the loss of the PCP protein Vangl2 in oligodendrocytes results in disruptions to the microtubule cytoskeleton and autotypic adhesions within the paranodal spiral of non-compact myelin, without perturbing the adhesion of this spiral to the axon. This has three major consequences for the underlying axon. First, a loss of the paranodal barrier resulting in disrupted axonal patterning surrounding nodes of Ranvier. Second, a local increase in paranodal axon diameter. Third, both decreased action potential thresholds and increased conduction velocity in the Vangl2 cKO CNS. These observations reveal that the PCP signalling molecule Vangl2 plays a key role in the sustaining the remarkable architecture of the paranode and so regulating impulse propagation in the CNS. Taken together with our prior work showing that loss of the apico-basal polarity protein Scribble causes the opposite phenotype – loss of axoglial adhesion within the spiral without perturbation of autotypic adhesions – our work suggests that orthogonal axes created by apico-basal and planar polarity pattern the adhesion molecules within the oligodendrocyte cytoplasmic channel to create the paranodal spiral.

This example of subcellular patterning mediated by polarity proteins working at orthogonal axes adds to our understanding as to how the paranodal axo-glial adhesions that pattern the axon at nodes of Ranvier are established. The central roles played by the axonal proteins Caspr and Contactin-1 as key constituents of these adhesions and the involvement of proteins such as ankyrin and spectrin family members in linking adhesion proteins to the axonal cytoskeleton has been extensively described in over past 15 years (reviewed by reviewed by reviewed by reviewed by reviewed by reviewed by reviewed by reviewed by C. Zhang & Rasband, 2016). In comparison, while NFC155 has been demonstrated to be the key oligodendroglial regulator of paranodal axo-glial adhesion, relatively little is known about other membrane and cytoskeletal proteins that organize paranodal myelin. The observation that fewer microtubules are present and that Claudin-11 is mislocalized within the paranodal channel in Vangl2 mutants is consistent with a model in which Vangl2 organizes the microtubule cytoskeleton, which is used to transport tight (and potentially other adhesion) junction proteins to their destinations within the paranodal spiral, where they contribute to its stability. Their loss leads to the loosened spiral observed in Vangl2 cKO CNS which, while maintaining contact with the axon, loses its barrier function as axonal nodal and juxtaparanodal complexes become mislocalized laterally along the axon. Loss of Vangl2 cKOs also compromises the organization of non-compact myelin itself, as septin filaments normally confined to the adaxonal internode invade the paranodes.

It is clear, however, that much remains to be learned about the mechanisms that organise the paranodal spiral. The phenotype observed in Vangl2 cKO CNS cannot be explained solely by disruption of Claudin-11. In the Claudin-11 null CNS, disruption to paranodes was not observed and impulse propagation is slowed and not hastened in these animals (Devaux & Gow, 2008; Maheras et al., 2018); its principal function is believed to be as a diffusion barrier for water and other small molecules (Denninger et al., 2015). One candidate for these additional effects in the Vangl2cKO mice is mislocalization of Cx32, which we were unable to examine by super resolution microscopy due to a lack of suitable antibodies. The primary role of Cx32 gap junctions in myelin is believed to be as a conduit permitting the transport of water, ions and other small molecules between turns of the paranodal spiral, and between abaxonal myelin and astrocytes, allowing for the buffering and recycling of K^+ ions released by neurons (Menichella et al., 2006). However, it has been reported that homotypic Cx32 interaction can drive cell-cell adhesion (Cotrina, Lin, & Nedergaard, 2008), and that enlarged and irregularly-shaped paranodal loops are present in the CNS of Cx32 null animals, with neurons in Cx32 mutant displaying hyperexcitability in response to weak stimuli (Sutor, Schmolke, Teubner, Schirmer, & Willecke, 2000). Given that Cx32 gap junctions are found only in oligodendrocytes, and that oligodendrocytes do not appear to form gap junctions with neurons (Rash, Yasumura, Dudek, & Nagy, 2001) these observations could indeed be consistent with this protein playing a role in organizing the paranodal spiral. While mice lacking both it and another oligodendroglial connexin, Cx47, experience a severe CNS phenotype including oligodendrocyte death and CNS demyelination, most likely due to a loss of astrocyte-oligodendrocyte gap junctions (Menichella, Goodenough, Sirkowski, Scherer, & Paul, 2003) Cx32 KO CNS does not show any gross myelin pathology(Scherer et al., 1998). A detailed analysis of myelin organization and axonal patterning at Cx32 KO nodes and paranodes could address the question of whether Cx32 plays an as-yet unidentified role in stabilizing the paranodal spiral in the CNS.

Other adhesion proteins may also play a role in stabilizing the paranodal spiral. In the PNS, E-cadherin is concentrated at adherens junctions between Schwann cell paranodal loops (Fannon et al., 1995). Vangl2 can bind directly to, and control the plasma membrane localization of, both E-cadherin (Nagaoka, Inutsuka, Begum, Bin hafiz, & Kishi, 2014) and N-cadherin (Nagaoka, Ohashi, et al., 2014). While E-cadherin is not expressed in oligodendroglia, N-cadherin is expressed in myelinating oligodendrocytes, where it plays a role in myelin initiation (Schnadelbach, Ozen, Blaschuk, Meyer, & Fawcett, 2001) highlighting this protein as an attractive candidate to mediate adhesion within paranodal spiral in the CNS. Another possible candidate for such a role in the CNS is the transmembrane protein opalin, which has been localized to sites between paranodal loops in CNS myelin (Yoshikawa et al., 2008). However conditional elimination of opalin in oligodendroglia does not affect paranodal organization or conduction, suggesting that it is not essential for the compaction of the paranodal spiral (Yoshikawa et al., 2016). Given the complexity of this structure, it seems likely that Vangl2 regulates the integrity of the paranodal spiral through the downstream actions of several redundant adhesion proteins, both known and yet to be identified. Finally, the possibility that that the observed mislocalization of Claudin-11 is a consequence, rather than a cause, of paranodal abnormalities in the Vangl2 cKO CNS cannot be dismissed. Null mutations in the gene encoding the axonal cytoskeletal protein Whirlin also result in paranodal loops trailing into the internode (Green, Yang, Grati, Kachar, & Bhat, 2013), as well as disrupted paranodal axo-glial adhesion and mis-localization of juxtaparanodal K_V channels to paranodes in older animals (Saifetiarova & Bhat, 2019), suggesting that the other causes of disruption to axo-glial interaction at the paranode may contribute to the observed trailing-loop phenotype.

A surprising insight gained through our study of the Vangl2 cKO phenotype relates to the ability of paranodal myelin to locally regulate axon diameter. The initial observation in CNS that axonal diameter is greatest at internodes and is decreased at the node of Ranvier and paranodes was made approximately 50 years ago (Hildebrand, 1971), and provides a mechanism to decrease the amount of energy that must be spent to repolarize the membrane following passing of an action potential. Both our own findings and those of Arancibia-Carcamo and colleagues suggest that sodium channel density appears to remain constant as the dimensions of the node of Ranvier change (Arancibia-Carcamo et al., 2017), suggesting that regulation of the amount of nodal membrane present is the primary factor in controlling the number of sodium ions that enter the nodal axon during depolarization. As restoration of membrane resting potential by the Na+/K+ ATPase is responsible for as much as 70% of the energy expenditure of neurons with long-projecting axons in the brain (Howarth, Gleeson, & Attwell, 2012), tightly controlling the dimensions of the node of Ranvier is an important mechanism that ensures that brain energy usage is efficient. However, the mechanism underlying nodal diameter reduction remains unknown. It has been observed in PNS that in cross-sections of internodal regions of myelinated axons, neurofilaments are relatively spread out, while they are more densely packed together at paranodes (Price, Lasek, & Katz, 1990) suggesting an external compressive force (Price, Lasek, & Katz, 1993). In the PNS, it was observed that a dense actin cytoskeleton encircles the paranodal axon, leading to the hypothesis that actin contractility within the Schwann cell generates force that squeezes the paranodal axon (Zimmermann, 1996). Vangl2 has a previously reported role in generating contractile force through regulation of the actin cytoskeleton during gastrulation (Ossipova, Chuykin, Chu, & Sokol, 2015), but as filamentous actin is largely absent from CNS myelin (Zuchero et al., 2015) any such compression would have to be driven by an actin-independent process. One possible interpretation of our findings is that increased paranodal axon diameter is consistent with an inability of the paranodal spiral to 'lock' by adhesion between loops at Vangl2 cKO CNS paranodes, leading to relaxation and lengthening of the spiral and an inability to squeeze the enlarging axon at paranodes as radial growth proceeds between P14 and P60. The presence of a compressive action of the paranodal spiral on the axon has not been proven at CNS or PNS nodes, however, and further investigation will be required to determine the mechanism by which Vangl2 regulates paranodal axon diameter.

We observed in the *Vangl2* cKO mice that the length of the Na_V-immunopositive domain was increased, extending into the paranode even though the length of the node as measured by electron microscopy was not altered. This lengthening presumably occurs through spiral diffusion of the channels along the widened areas of axon membrane created between turns of the loosened paranodal loops - the so-called 'pathway 3' described by Mierzwa in 2010 (Mierzwa, Shroff, & Rosenbluth, 2010). This in turn may explain why nerves lacking oligodendroglial Vangl2 expression show increased conduction velocities despite internodal lengths in Vangl2 cKO teased spinal cord fibres not varying significantly from wild-type (data not shown). Mathematical modelling of conduction along myelinated CNS axons predicts that the length of nodes of Ranvier (and therefore the length of the Na_V-immunopositive domain in normal mice) is a key parameter that influences conduction velocity (Arancibia-Carcamo et al., 2017). Using the computer model published by Arancibia-Carcamo et al., using our measured length of the Na_V-immunopositive domain in the *Vangl2* cKO mice (Fig. 4H) as the nodal length predicts an increase in conduction velocity (Values used: Nodal diameter: WT: 0.88 μm, cKO: 0.88; Nodal length: WT: 1.95 μm, cKO: 3.18 μm; Internodal length: WT: 576.5 μm, cKO: 500.6 μm; Internodal diameter: WT: 3.45 μm, cKO: 3.75 μm; g-ratio: WT: 0.759, cKO: 0.753; Predicted conduction velocity: WT: 11.85 m/s, cKO: 14.20 m/s), consistent with the results of our electrophysiological studies. A key assumption of this model, however, is that the density of sodium channels at the nodal plasma membrane is held constant. Indeed, we found that no significant difference in the mean intensity of nodal Na_V immunofluorescence could be observed in Vangl2 cKO teased spinal cord at P60, suggesting that the functionally longer nodes of Ranvier in the Vangl2 cKO contain more voltage-gated sodium channels than do those in wild-type CNS. Implicit in our assumption is that the entire sodium channel domain (and not just the region of bare axon between adjacent myelin segments) contributes to conduction in Vangl2 cKO, with the sodium channels mislocalized into paranodal regions in these animals accessible and actively contributing to depolarization.

Our results showing increased conduction velocity with loss of loop-loop adhesion differs from that reported for animals lacking another paranodal autotypic adhesion molecule, JAM-C (Scheiermann et al., 2007). Here decreased conduction is seen in the PNS of JAM-C deficient mice. However, a deficiency of JAM-C causes a loss of both loop-loop and loop-axon adhesion, as shown in Figures 2B and S4D of that paper. We suggest that there will be a much greater perturbation of the paranodal sealing required for saltatory conduction resulting from loss of adhesion between loops and the underlying axon than from a loop-loop defect, and that this loss of sealing then dominates the electrophysiological phenotype.

A predicted consequence of an increased number of sodium channels at Vangl2 cKO nodes of Ranvier would be a corresponding increase in the amount of energy required to repolarize the membrane following passing of an action potential. Interestingly and consistent with this, we observed that an increased proportion of nodes of Ranvier in Vangl2 cKO P60 spinal cord contained mitochondria compared to wild-type nodes (data not shown), which could represent a response to this increased metabolic demand of the Na^+/K^+ ATPase as has been observed in the peripheral nervous system (PNS,C. L. Zhang, Ho, Kintner, Sun, & Chiu, 2010). Increased energy demand by axons could also explain why myelin sheaths in P60 Vangl2 cKO spinal cord contain significantly more internodal Schmidt-Lanterman incisure-like myelinic channels (data not shown), as these structures are thought to play a key role in delivering metabolic support from the oligodendrocyte to the axon (Philips & Rothstein, 2017).

Finally, our finding that Vangl2 is a key regulator of paranodal architecture also has important implications for myelin pathology and plasticity. Paranodal loosening occurs with CNS aging (Hinman et al., 2006) and elongation of paranodes has been observed in regions of the brain that have undergone remyelination in multiple sclerosis patients (Howell et al., 2006). The similarity of these phenotypes with those we see here suggests that Vangl2 may be compromised in ageing or disease. Such a conclusion is potentially important, as a possible consequence of 'looser' paranodal assembly could be increased susceptibility of the myelin sheath to age-related demyelination, or to further damage following remyelination, at least in part due to the presence of circulating antibodies in the sera of individuals suffering from multiple sclerosis recognizing paranodal epitopes that are normally inaccessible (Mathey et al., 2007). This could for example provide an explanation for why MS lesions often re-occur in regions where lesions have already occurred (Prineas et al., 1993).

REFERENCES

Amor, V., Zhang, C., Vainshtein, A., Zhang, A., Zollinger, D. R., Eshed-Eisenbach, Y., . . . Peles, E. (2017). The paranodal cytoskeleton clusters Na(+) channels at nodes of Ranvier. *Elife, 6*. doi:10.7554/eLife.21392

Anitei, M., Ifrim, M., Ewart, M. A., Cowan, A. E., Carson, J. H., Bansal, R., & Pfeiffer, S. E. (2006). A role for Sec8 in oligodendrocyte morphological differentiation. *J.Cell Sci., 119*(Pt 5), 807-818. Retrieved from PM:16478790

Arancibia-Carcamo, I. L., Ford, M. C., Cossell, L., Ishida, K., Tohyama, K., & Attwell, D. (2017). Node of Ranvier length as a potential regulator of myelinated axon conduction speed. *Elife, 6*. doi:10.7554/eLife.23329

Bhat, M. A., Rios, J. C., Lu, Y., Garcia-Fresco, G. P., Ching, W., St Martin, M., . . . Bellen, H. J. (2001). Axon-glia interactions and the domain organization of myelinated axons requires neurexin IV/Caspr/Paranodin. *Neuron, 30*(2), 369-383. Retrieved from PM:11395000

Bilder, D., & Perrimon, N. (2000). Localization of apical epithelial determinants by the basolateral PDZ protein Scribble. *Nature, 403*(6770), 676-680. Retrieved from PM:10688207

Boison, D., Bussow, H., Durso, D., Muller, H. W., & Stoffel, W. (1995). Adhesive Properties of Proteolipid Protein Are Responsible for the Compaction of Cns Myelin Sheaths. *Journal of Neuroscience, 15*(8), 5502-5513. Retrieved from ISI:A1995RP56000007

Campanale, J. P., Sun, T. Y., & Montell, D. J. (2017). Development and dynamics of cell polarity at a glance. *J Cell Sci, 130*(7), 1201-1207. doi:10.1242/jcs.188599

Charles, P., Tait, S., Faivre-Sarrailh, C., Barbin, G., Gunn-Moore, F., Denisenko-Nehrbass, N., . . . Lubetzki, C. (2002). Neurofascin is a glial receptor for the paranodin/Caspr-contactin axonal complex at the axoglial junction. *Curr.Biol., 12*(3), 217-220. Retrieved from PM:11839274

Chen, H., Xiao, X., Lui, W. Y., Lee, W. M., & Cheng, C. Y. (2018). Vangl2 regulates spermatid planar cell polarity through microtubule (MT)-based cytoskeleton in the rat testis. *Cell Death Dis, 9*(3), 340. doi:10.1038/s41419-018-0339-x

Cotrina, M. L., Lin, J. H., & Nedergaard, M. (2008). Adhesive properties of connexin hemichannels. *Glia, 56*(16), 1791-1798. doi:10.1002/glia.20728

Courbard, J. R., Djiane, A., Wu, J., & Mlodzik, M. (2009). The apical/basal-polarity determinant Scribble cooperates with the PCP core factor Stbm/Vang and functions as one of its effectors. *Dev Biol, 333*(1), 67-77. doi:10.1016/j.ydbio.2009.06.024

Denninger, A. R., Breglio, A., Maheras, K. J., LeDuc, G., Cristiglio, V., Deme, B., . . . Kirschner, D. A. (2015). Claudin-11 Tight Junctions in Myelin Are a Barrier to Diffusion and Lack Strong Adhesive Properties. *Biophys J, 109*(7), 1387-1397. doi:10.1016/j.bpj.2015.08.012

Devaux, J., & Gow, A. (2008). Tight junctions potentiate the insulative properties of small CNS myelinated axons. *J Cell Biol, 183*(5), 909-921. doi:10.1083/jcb.200808034

Dos-Santos Carvalho, S., Moreau, M. M., Hien, Y. E., Garcia, M., Aubailly, N., Henderson, D. J., . . . Montcouquiol, M. (2020). Vangl2 acts at the interface between actin and N-cadherin to modulate mammalian neuronal outgrowth. *Elife, 9*. doi:10.7554/eLife.51822

Fannon, A. M., Sherman, D. L., Ilyina-Gragerova, G., Brophy, P. J., Friedrich, V. L., Jr., & Colman, D. R. (1995). Novel E-cadherin-mediated adhesion in peripheral nerve: Schwann cell architecture is stabilized by autotypic adherens junctions. *J.Cell Biol., 129*(1), 189-202. Retrieved from PM:7698985

Ferreira T, H. M., Rueden C, Miura K, Eglinger J, Chef B. (2017). tferr/Scripts: BAR 1.5.1 (Version 1.51). http://doi.org/10.5281/zenodo.495245.

Foster, R. E., Connors, B. W., & Waxman, S. G. (1982). Rat optic nerve: electrophysiological, pharmacological and anatomical studies during development. *Brain Res, 255*(3), 371-386. Retrieved from http://www.ncbi.nlm.nih.gov/pubmed/7066695

Fünfschilling, U., Supplie, L., Mahad, D., Boretius, S., Saab, A., Edgar, J., . . . Nave, K.-A. (2012). Glycolytic oligodendrocytes maintain myelin and long-term axonal integrity. *Nature, 485*(7399), 517-538. doi:10.1038/nature11007

Glotfelty, L. G., Zahs, A., Iancu, C., Shen, L., & Hecht, G. A. (2014). Microtubules are required for efficient epithelial tight junction homeostasis and restoration. *Am J Physiol Cell Physiol, 307*(3), C245-254. doi:10.1152/ajpcell.00336.2013

Gow, A., Southwood, C. M., Li, J. S., Pariali, M., Riordan, G. P., Brodie, S. E., . . . Lazzarini, R. A. (1999). CNS myelin and sertoli cell tight junction strands are absent in Osp/claudin-11 null mice. *Cell, 99*(6), 649-659. Retrieved from PM:10612400

Green, J. A., Yang, J., Grati, M., Kachar, B., & Bhat, M. A. (2013). Whirlin, a cytoskeletal scaffolding protein, stabilizes the paranodal region and axonal cytoskeleton in myelinated axons. *BMC Neurosci, 14*, 96. doi:10.1186/1471-2202-14-96

Hildebrand, C. (1971). Ultrastructural and light-microscopic studies of the nodal region in large myelinated fibres of the adult feline spinal cord white matter. *Acta Physiol Scand Suppl, 364*, 43-79. Retrieved from http://www.ncbi.nlm.nih.gov/pubmed/4109394

Hildebrand, C., & Skoglund, S. (1971). Calibre spectra of some fibre tracts in the feline central nervous system during postnatal development. *Acta Physiol Scand Suppl, 364*, 5-41. Retrieved from http://www.ncbi.nlm.nih.gov/pubmed/4109395

Hinman, J. D., Peters, A., Cabral, H., Rosene, D. L., Hollander, W., Rasband, M. N., & Abraham, C. R. (2006). Age-related molecular reorganization at the node of Ranvier. *J Comp Neurol, 495*(4), 351-362. doi:10.1002/cne.20886

Howarth, C., Gleeson, P., & Attwell, D. (2012). Updated energy budgets for neural computation in the neocortex and cerebellum. *J Cereb Blood Flow Metab, 32*(7), 1222-1232. doi:10.1038/jcbfm.2012.35

Howell, O. W., Palser, A., Polito, A., Melrose, S., Zonta, B., Scheiermann, C., . . . Reynolds, R. (2006). Disruption of neurofascin localization reveals early changes preceding demyelination and remyelination in multiple sclerosis. *Brain, 129*(Pt 12), 3173-3185. Retrieved from http://www.ncbi.nlm.nih.gov/entrez/query.fcgi?cmd=Retrieve&db=PubMed&dopt=Citation&list_uids=17041241

Huxley, A. F., & Stampfli, R. (1949). Evidence for saltatory conduction in peripheral myelinated nerve fibres. *J Physiol, 108*(3), 315-339. Retrieved from https://www.ncbi.nlm.nih.gov/pubmed/18144923

Jarjour, A. A., Boyd, A., Dow, L. E., Holloway, R. K., Goebbels, S., Humbert, P. O., . . . ffrench-Constant, C. (2015). The polarity protein Scribble regulates myelination and remyelination in the central nervous system. *PLoS Biol, 13*(3), e1002107. doi:10.1371/journal.pbio.1002107

Kamasawa, N., Sik, A., Morita, M., Yasumura, T., Davidson, K. G., Nagy, J. I., & Rash, J. E. (2005). Connexin-47 and connexin-32 in gap junctions of oligodendrocyte somata, myelin sheaths, paranodal loops and Schmidt-Lanterman incisures: implications for ionic homeostasis and potassium siphoning. *Neuroscience, 136*(1), 65-86. Retrieved from PM:16203097

Lappe-Siefke, C., Goebbels, S., Gravel, M., Nicksch, E., Lee, J., Braun, P. E., . . . Nave, K. A. (2003). Disruption of Cnp1 uncouples oligodendroglial functions in axonal support and myelination. *Nat.Genet., 33*(3), 366-374. Retrieved from PM:12590258

Lee, Y., Morrison, B. M., Li, Y., Lengacher, S., Farah, M. H., Hoffman, P. N., . . . Rothstein, J. D. (2012). Oligodendroglia metabolically support axons and contribute to neurodegeneration. *Nature, 487*(7408), 443-448. doi:10.1038/nature11314

Leung, V., Iliescu, A., Jolicoeur, C., Gravel, M., Apuzzo, S., Torban, E., . . . Gros, P. (2016). The planar cell polarity protein Vangl2 is required for retinal axon guidance. *Dev Neurobiol, 76*(2), 150-165. doi:10.1002/dneu.22305

Liu, C., Lin, C., Whitaker, D. T., Bakeri, H., Bulgakov, O. V., Liu, P., . . . Swaroop, A. (2013). Prickle1 is expressed in distinct cell populations of the central nervous system and contributes to neuronal morphogenesis. *Hum Mol Genet, 22*(11), 2234-2246. doi:10.1093/hmg/ddt075

Maheras, K. J., Peppi, M., Ghoddoussi, F., Galloway, M. P., Perrine, S. A., & Gow, A. (2018). Absence of Claudin 11 in CNS Myelin Perturbs Behavior and Neurotransmitter Levels in Mice. *Sci Rep, 8*(1), 3798. doi:10.1038/s41598-018-22047-9

Mathey, E. K., Derfuss, T., Storch, M. K., Williams, K. R., Hales, K., Woolley, D. R., . . . Linington, C. (2007). Neurofascin as a novel target for autoantibody-mediated axonal injury. *J Exp Med, 204*(10), 2363-2372. doi:10.1084/jem.20071053

Menichella, D. M., Goodenough, D. A., Sirkowski, E., Scherer, S. S., & Paul, D. L. (2003). Connexins are critical for normal myelination in the CNS. *J Neurosci, 23*(13), 5963-5973. Retrieved from http://www.ncbi.nlm.nih.gov/pubmed/12843301

Menichella, D. M., Majdan, M., Awatramani, R., Goodenough, D. A., Sirkowski, E., Scherer, S. S., & Paul, D. L. (2006). Genetic and physiological evidence that oligodendrocyte gap junctions contribute to spatial buffering of potassium released during neuronal activity. *J Neurosci, 26*(43), 10984-10991. doi:10.1523/JNEUROSCI.0304-06.2006

Mierzwa, A., Shroff, S., & Rosenbluth, J. (2010). Permeability of the paranodal junction of myelinated nerve fibers. *J Neurosci, 30*(47), 15962-15968. doi:10.1523/JNEUROSCI.4047-10.2010

Montcouquiol, M., Rachel, R. A., Lanford, P. J., Copeland, N. G., Jenkins, N. A., & Kelley, M. W. (2003). Identification of Vangl2 and Scrb1 as planar polarity genes in mammals. *Nature, 423*(6936), 173-177. Retrieved from PM:12724779

Nagaoka, T., Inutsuka, A., Begum, K., Bin hafiz, K., & Kishi, M. (2014). Vangl2 regulates E-cadherin in epithelial cells. *Sci Rep, 4*, 6940. doi:10.1038/srep06940

Nagaoka, T., Ohashi, R., Inutsuka, A., Sakai, S., Fujisawa, N., Yokoyama, M., . . . Kishi, M. (2014). The Wnt/planar cell polarity pathway component Vangl2 induces synapse formation through direct control of N-cadherin. *Cell Rep, 6*(5), 916-927. doi:10.1016/j.celrep.2014.01.044

Okerlund, N. D., Stanley, R. E., & Cheyette, B. N. (2016). The Planar Cell Polarity Transmembrane Protein Vangl2 Promotes Dendrite, Spine and Glutamatergic Synapse Formation in the Mammalian Forebrain. *Mol Neuropsychiatry, 2*(2), 107-114. doi:10.1159/000446778

Ossipova, O., Chuykin, I., Chu, C. W., & Sokol, S. Y. (2015). Vangl2 cooperates with Rab11 and Myosin V to regulate apical constriction during vertebrate gastrulation. *Development, 142*(1), 99-107. doi:10.1242/dev.111161

Patzig, J., Erwig, M. S., Tenzer, S., Kusch, K., Dibaj, P., Mobius, W., . . . Werner, H. B. (2016). Septin/anillin filaments scaffold central nervous system myelin to accelerate nerve conduction. *Elife, 5*. doi:10.7554/eLife.17119

Philips, T., & Rothstein, J. D. (2017). Oligodendroglia: metabolic supporters of neurons. *J Clin Invest, 127*(9), 3271-3280. doi:10.1172/JCI90610

Price, R. L., Lasek, R. J., & Katz, M. J. (1990). Internal axonal cytoarchitecture is shaped locally by external compressive forces. *Brain Res, 530*(2), 205-214. Retrieved from http://www.ncbi.nlm.nih.gov/pubmed/1702341

Price, R. L., Lasek, R. J., & Katz, M. J. (1993). Neurofilaments assume a less random architecture at nodes and in other regions of axonal compression. *Brain Res, 607*(1-2), 125-133. Retrieved from http://www.ncbi.nlm.nih.gov/pubmed/8481791

Prineas, J. W., Barnard, R. O., Revesz, T., Kwon, E. E., Sharer, L., & Cho, E. S. (1993). Multiple sclerosis. Pathology of recurrent lesions. *Brain, 116 (Pt 3)*, 681-693. Retrieved from http://www.ncbi.nlm.nih.gov/pubmed/8513397

Ramsbottom, S. A., Sharma, V., Rhee, H. J., Eley, L., Phillips, H. M., Rigby, H. F., . . . Henderson, D. J. (2014). Vangl2-regulated polarisation of second heart field-derived cells is required for outflow tract lengthening during cardiac development. *PLoS Genet, 10*(12), e1004871. doi:10.1371/journal.pgen.1004871

Rash, J. E., Yasumura, T., Dudek, F. E., & Nagy, J. I. (2001). Cell-specific expression of connexins and evidence of restricted gap junctional coupling between glial cells and between neurons. *J Neurosci, 21*(6), 1983-2000. Retrieved from http://www.ncbi.nlm.nih.gov/pubmed/11245683

Rios, J. C., Melandez-Vasquez, C. V., Einheber, S., Lustig, M., Grumet, M., Hemperly, J., . . . Salzer, J. L. (2000). Contactin-associated protein (Caspr) and contactin form a complex that is targeted to the paranodal junctions during myelination. *Journal of Neuroscience, 20*(22), 8354-8364. Retrieved from ISI:000165131500020

Saifetiarova, J., & Bhat, M. A. (2019). Ablation of cytoskeletal scaffolding proteins, Band 4.1B and Whirlin, leads to cerebellar purkinje axon pathology and motor dysfunction. *J Neurosci Res, 97*(3), 313-331. doi:10.1002/jnr.24352

Sanchez, I., Hassinger, L., Paskevich, P. A., Shine, H. D., & Nixon, R. A. (1996). Oligodendroglia regulate the regional expansion of axon caliber and local accumulation of neurofilaments during development independently of myelin formation. *J Neurosci, 16*(16), 5095-5105. Retrieved from http://www.ncbi.nlm.nih.gov/pubmed/8756439

Sargiannidou, I., Vavlitou, N., Aristodemou, S., Hadjisavvas, A., Kyriacou, K., Scherer, S. S., & Kleopa, K. A. (2009). Connexin32 mutations cause loss of function in Schwann cells and oligodendrocytes leading to PNS and CNS myelination defects. *J Neurosci, 29*(15), 4736-4749. doi:10.1523/JNEUROSCI.0325-09.2009

Scheiermann, C., Meda, P., Aurrand-Lions, M., Madani, R., Yiangou, Y., Coffey, P., . . . Nourshargh, S. (2007). Expression and function of junctional adhesion molecule-C in myelinated peripheral nerves. *Science, 318*(5855), 1472-1475. doi:10.1126/science.1149276

Scherer, S. S., Xu, Y. T., Nelles, E., Fischbeck, K., Willecke, K., & Bone, L. J. (1998). Connexin32-null mice develop demyelinating peripheral neuropathy. *Glia, 24*(1), 8-20. Retrieved from http://www.ncbi.nlm.nih.gov/pubmed/9700485

Schindelin, J., Arganda-Carreras, I., Frise, E., Kaynig, V., Longair, M., Pietzsch, T., . . . Cardona, A. (2012). Fiji: an open-source platform for biological-image analysis. *Nat Methods, 9*(7), 676-682. doi:10.1038/nmeth.2019

Schnadelbach, O., Ozen, I., Blaschuk, O. W., Meyer, R. L., & Fawcett, J. W. (2001). N-cadherin is involved in axon-oligodendrocyte contact and myelination. *Mol Cell Neurosci, 17*(6), 1084-1093. doi:10.1006/mcne.2001.0961

Simons, M., Snaidero, N., & Aggarwal, S. (2012). Cell polarity in myelinating glia: from membrane flow to diffusion barriers. *Biochim Biophys Acta, 1821*(8), 1146-1153. doi:S1388-1981(12)00016-9 [pii]

10.1016/j.bbalip.2012.01.011

Sun, S. D., Purdy, A. M., & Walsh, G. S. (2016). Planar cell polarity genes Frizzled3a, Vangl2, and Scribble are required for spinal commissural axon guidance. *BMC Neurosci, 17*(1), 83. doi:10.1186/s12868-016-0318-z

Sutor, B., Schmolke, C., Teubner, B., Schirmer, C., & Willecke, K. (2000). Myelination defects and neuronal hyperexcitability in the neocortex of connexin 32-deficient mice. *Cereb Cortex, 10*(7), 684-697. Retrieved from http://www.ncbi.nlm.nih.gov/pubmed/10906315

Tasaki, I., & Takeuchi, T. J. P. s. A. f. d. g. P. d. M. u. d. T. (1942). Weitere Studien über den Aktionsstrom der markhaltigen Nervenfaser und über die elektrosaltatorische Übertragung des Nervenimpulses. *245*(5), 764-782. doi:10.1007/bf01755237

Thakar, S., Wang, L., Yu, T., Ye, M., Onishi, K., Scott, J., . . . Zou, Y. (2017). Evidence for opposing roles of Celsr3 and Vangl2 in glutamatergic synapse formation. *Proc Natl Acad Sci U S A, 114*(4), E610-E618. doi:10.1073/pnas.1612062114

Yates, L. L., Schnatwinkel, C., Hazelwood, L., Chessum, L., Paudyal, A., Hilton, H., . . . Dean, C. H. (2013). Scribble is required for normal epithelial cell-cell contacts and lumen morphogenesis in the mammalian lung. *Dev Biol, 373*(2), 267-280. doi:10.1016/j.ydbio.2012.11.012

Yoshikawa, F., Sato, Y., Tohyama, K., Akagi, T., Furuse, T., Sadakata, T., . . . Furuichi, T. (2016). Mammalian-Specific Central Myelin Protein Opalin Is Redundant for Normal Myelination: Structural and Behavioral Assessments. *PLoS One, 11*(11), e0166732. doi:10.1371/journal.pone.0166732

Yoshikawa, F., Sato, Y., Tohyama, K., Akagi, T., Hashikawa, T., Nagakura-Takagi, Y., . . . Furuichi, T. (2008). Opalin, a transmembrane sialylglycoprotein located in the central nervous system myelin paranodal loop membrane. *J Biol Chem, 283*(30), 20830-20840. doi:10.1074/jbc.M801314200

Yuan, J., Cha, J., Deng, W., Bartos, A., Sun, X., Ho, H. H., . . . Dey, S. K. (2016). Planar cell polarity signaling in the uterus directs appropriate positioning of the crypt for embryo implantation. *Proc Natl Acad Sci U S A, 113*(50), E8079-E8088. doi:10.1073/pnas.1614946113

Zhang, C., & Rasband, M. N. (2016). Cytoskeletal control of axon domain assembly and function. *Curr Opin Neurobiol, 39*, 116-121. doi:10.1016/j.conb.2016.05.001

Zhang, C. L., Ho, P. L., Kintner, D. B., Sun, D., & Chiu, S. Y. (2010). Activity-dependent regulation of mitochondrial motility by calcium and Na/K-ATPase at nodes of Ranvier of myelinated nerves. *J Neurosci, 30*(10), 3555-3566. doi:10.1523/JNEUROSCI.4551-09.2010

Zilkha-Falb, R., Gurevich, M., Hanael, E., & Achiron, A. (2017). Prickle1 as positive regulator of oligodendrocyte differentiation. *Neuroscience, 364*, 107-121. doi:10.1016/j.neuroscience.2017.09.018

Zimmermann, H. (1996). Accumulation of synaptic vesicle proteins and cytoskeletal specializations at the peripheral node of Ranvier. *Microscopy Research and Technique, 34*(5), 462-473. Retrieved from ISI:A1996UY76300007

Zollinger, D. R., Baalman, K. L., & Rasband, M. N. (2015). The ins and outs of polarized axonal domains. *Annu Rev Cell Dev Biol, 31*, 647-667. doi:10.1146/annurev-cellbio-100913-013107

Zonta, B., Tait, S., Melrose, S., Anderson, H., Harroch, S., Higginson, J., . . . Brophy, P. J. (2008). Glial and neuronal isoforms of Neurofascin have distinct roles in the assembly of nodes of Ranvier in the central nervous system. *J.Cell Biol.* Retrieved from PM:18573915

Zuchero, J. B., Fu, M. M., Sloan, S. A., Ibrahim, A., Olson, A., Zaremba, A., . . . Barres, B. A. (2015). CNS myelin wrapping is driven by actin disassembly. *Dev Cell, 34*(2), 152-167. doi:10.1016/j.devcel.2015.06.011

FIGURE LEGENDS

Figure 1. Organization of the CNS myelin sheath.

A: Myelin sheaths produced by oligodendrocytes consist of compacted layers of plasma membrane wrapped around the axon. The lateral edge of each sheath, which abuts the node of Ranvier (light pink) is characterized by a cytoplasm-filled channel that spirals around the paranodal axon (yellow), separating the node from the juxtaparanode (orange). The channel continues with a trajectory roughly parallel to the axon into the internodal axon (red). On the right is a partially-unfurled myelin sheath, showing the division between compact myelin (dark blue) and the cytoplasmic channel (light blue). B,C: A longitudinal cross-section of the paranode reveals that the spiral appears as a series of cytoplasm-filled loops that are adhere to both the axon and each other. The adhesions present in each paranodal loops, and the polarity of the axis along which these adhesion complexes are patterned, are shown in C. D,E: Paranodal axo-glial adhesions are disrupted in the CNS following conditional elimination of *Scribble* expression in oligodendroglia.

Figure 2. Elimination of Vangl2 expression in CNP-Cre:Vangl2$^{fl/fl}$ oligodendrocytes and paranodes.

Cultures derived from Vangl2 WT mice and differentiated for two days show expression of Vangl2 protein (A,B, green) by oligodendrocytes expressing myelin basic protein (MBP, B, red). Vangl2 protein is almost entirely absent from oligodendrocyte cultures derived from Vangl2 cKO mice (C,D). Similarly, Vangl2 protein (E,F, green) is present at paranodes labelled for Caspr (F, red) in P60 teased spinal cord fibres from Vangl2 WT mice, but not in teased fibre preparations from Vangl2 cKO mice (G,H). Scale bars: (A-D): 5 µm, (E-H): 3 µm.

Figure 3. Disruption of the paranodal spiral in the Vangl2 conditional mutant CNS.

A-D: The paranodal spiral is disrupted in Vangl2 cKO CNS. Caspr immunolabelling (green) extends away from NaV immunolabelling (red), into the internode in Vangl2 cKO CNS (B,D), forming a looser (trailing) spiral than observed in wild-type controls (A,C). Note that the portion of the paranodal spiral closest to the node remains tightly wound, as evidenced by solid Caspr immunostaining. In panels C and D, the axon is immunolabelled for the 200 kDA neurofilament subunit (NFH, blue). The percentage of these paranodes with trailing Caspr was significantly increased (E, WT: 8.8±1.9, cKO: 30.3±4.4, p=0.0079). F: Electron microscopy reveals the presence of aberrant cytoplasm-filled myelin loops in internodal myelin in Vangl2 cKO spinal cord at P60 (F, arrows). G-J: Paranodal loops largely remain adhered to the axonal surface in the Vangl2 cKO CNS (I), as in wild-type CNS (G, quantification in H, Percentage of paranodal loops disengaged from the axonal surface: WT: 14.0±2.8, cKO: 21.6±2.4, p=0.0952). An increase in the percentage of paranodal loops that were separated from each other was observed in Vangl2 cKO spinal cord (I, arrowheads), relative to wild-type (G, quantification in J, Percentage of interfaces between neighbouring paranodal loops showing separation: WT: 20.9±1.6, cKO: 39.0±4.0, p=0.0079). K-N: Superresolution gSTED confocal imaging of the Caspr spiral further revealed that spacing between turns of the paranodal spiral is increased in Vangl2 cKO teased spinal cord fibres at P60 (M) relative to wild-type paranodes (K, quantification in L,N; Mean distance between turns of the paranodal spiral: WT: 419.5±9.2 nm, cKO: 479.2±16.4 nm, $p = 0.016$; Equation of best-fit line: WT: $y=13.8\pm2.5x + 375.5\pm10.0$, cKO: $y=31.5\pm3.1x + 370.1\pm13.4$, $p < 0.0001$ (slope)). All data are represented as mean ± SEM. $n = 5$ mice per genotype. Statistical analyses were performed using the Mann-Whitney test. A-E: At least 40 paranodes were analysed per animal. G-K, K-N: At least 20 paranodes were analysed per animal. Scale bars (A-D): 5 µm, (G,I): 250 nm, (K,M): 1 µm.

Figure 4. Oligodendroglial Vangl2 expression is required for domain organization of myelinated CNS axons at nodes of Ranvier.

In wild-type CNS, Caspr-immunopositive paranodes (green) flank Na_V-immunopositive nodes of Ranvier (red), with a clear separation existing between neighbouring paranodes (A,C,E). In Vangl2 cKO CNS (B,D,F) the Caspr domain extends both into the internode (B, arrowhead) and into the node of Ranvier (B, arrow). This shortens the node (quantified in G, distance between paranodal Caspr immunolabelling across node of Ranvier (μm): WT: 1.34±0.08, cKO: 0.90±0.05, p=0.0079). The nodal Na_V-immunolabelled domain is widened and spreads laterally into the paranodes (D, arrowheads, quantified in H; width of nodal Na_V immunolabelling (μm): WT: 1.9±0.1, cKO: 3.2±0.2, p=0.0079). No significant change in nodal sodium channel immunolabelling intensity was observed in Vangl2 cKO CNS (I; WT: 100.8±10.6, cKO: 94.4±6.4, p = 0.8413). In wild-type CNS, a clear paranodal separation is observed between nodal Na_V (red) and juxtaparanodal K_V (green) immunolabeling (J,L,N). In Vangl2 cKO (K,M,O), the K_V-immunolabeled area is widened (P; width of $K_V1.1$ immunolabelling (μm): WT: 17.8±1.0, cKO: 28.9±3.2, p=0.0079) and invades the paranodal domain (K, O, arrowheads), with the distance between Na_V and $K_V1.1$ immunolabelling reduced (Q; WT: 2.5±0.2μm, cKO: 1.5±0.2μm, p=0.0159). (Q-AA): Septin-8 is mislocalized to paranodes in Vangl2 cKO P60 teased spinal cord fibres. Septin-8 (green), which is restricted to the internodal inner tongue in wild-type fibres (R,T,V), extends into Caspr-immunopositive (red) paranodal regions in Vangl2 cKO fibres (S,U,W, arrowheads), with the percentage length of the Caspr-immunopositive domain that overlapped with Septin-8 labelling being significantly increased (X; WT: 19.6±3.7, cKO: 35.3±3.1, p=0.0317). Myelin was immunolabelled for MAG (blue) and axons for NFH (white). Superresolution imaging using gated STED reveals that Septin-8 (green, Y,AA) and Caspr (red, Z,AA) do not co-localise at paranodes. All data are represented as mean ± SEM. n = 5 mice per genotype. Statistical analyses were performed using the Mann-Whitney test. A-H: At least 20 nodes of Ranvier were analysed per animal. I-P: At least 40 paranodes were analysed per animal. Scale bars: (A-F and J-O): 5 µm, (Y-AA): 300 nm.

Figure 5. Vangl2 is required for local regulation of axon diameter in myelinated CNS axons.

In wild-type spinal cord at P60 (A), paranodal axon diameter (dP) is smaller than internodal diameter (dI). A relative increase in dP is observed in Vangl2 cKO spinal cord at P60 (B), resulting in an increased dP/dI ratio relative to that observed in wild-type controls (E; WT: 0.73±0.02, cKO: 0.77±0.02, p=0.0157). dP/dI ratio is not significantly different between Vangl2 WT and cKO in P14 spinal cord (C,D,F; WT: 0.84±0.02, cKO: 0.81±0.02, p=0.2222). All data are represented as mean ± SEM. n = 5 mice per genotype. Statistical analyses were performed using the Mann-Whitney test. At least 25 paranodes were analysed per animal, per time point. Scale bars: (A,B) and (C,D): 500 nm.

Figure 6. Loss of Vangl2 expression by oligodendrocytes increases the conductivity of myelinated CNS axons.

A representative compound action potential (CAP) recording showing three peaks is shown in (A). The first component is labelled with a black arrowhead, the second with a black arrow, and the third with a grey arrow. The double-headed arrows represent latency, which is measured as the time between the stimulus artefact (asterisk) and the negative peak of each triphasic component. The mean conduction velocity of the three CAP peaks is increased in Vangl2 cKO optic nerve (B; 1st component: WT: 2.47±0.26 m/s, cKO: 3.23±0.23; 2nd component: WT: 1.14±0.11, cKO: 1.37±0.10; 3rd component: WT: 0.57±0.06, cKO: 0.75±0.03, $p = 0.0047$). The mean minimum stimulus intensity at which each component of the CAP was first detected was decreased in Vangl2 cKO optic nerve, as shown by representative traces (C, quantification in D; 1st component: WT: 18.9±4.6 µA, cKO: 11.4±2.2; 2nd component: WT: 16.4±1.4, cKO: 12.9±1.8; 3rd component: WT: 42.1±3.2, cKO: 32.1±4.7, $p = 0.0123$). Statistical analyses were performed using two-way ANOVA followed by Sidak’s multiple comparisons test (B,D). $N = 7$ nerves from four animals per genotype.

Figure 7. Vangl2 controls the distribution of the autotypic tight junction protein Claudin-11 within CNS paranodal myelin.

(A-I): Standard and superresolution gated stimulation emission depletion (gSTED) confocal microscopy revealed altered distribution of Claudin-11 in P60 Vangl2 cKO spinal cord paranodes. The spiral of paranodal oligodendroglial Claudin-11 immunolabelling is loosened and elongated laterally along the axon in teased spinal cord preparations from Vangl2 cKO mice (B) relative to those from Vangl2 WT (A). In Vangl2 cKO paranodes (D,F), the intensity of Claudin-11 distribution (red in C,D, white in E,F) appeared diffuse relative to that observed in wild-type paranodes (C,E). Caspr-immunolabelled axo-glial adhesions are shown in green (C,D). When Claudin-11 immunolabelling intensity is plotted across individual paranodes (along the yellow lines in E and F), analysis of intensity maxima (red dots in G,I and minima (blue dots in G,I) revealed that the difference between maxima and minima was decreased at Vangl2 cKO paranodes (H). (J-L): Microtubule density is reduced in the Vangl2 cKO paranodal spiral. In P60 Vangl2 cKO spinal cord (L), the density of microtubules (white arrowheads) within paranodal loops was decreased relative to that observed in wild-type animals (J, quantification in K; WT: 129.5±10.2 microtubules/μm^2, cKO: 51.6±5.4 microtubules/μm^2, p=0.0079). All data are represented as mean ± SEM. n = 5 mice per genotype. (C-I): At least 20 paranodes were analysed per animal. (J-L): At least 50 paranodal loops from at least 10 paranodes were analysed per animal. Statistical analyses were performed using the Mann-Whitney test. Scale bars: (A,B): 5 µm ,(C-F): 1 µm, (J,L): 200 nm.

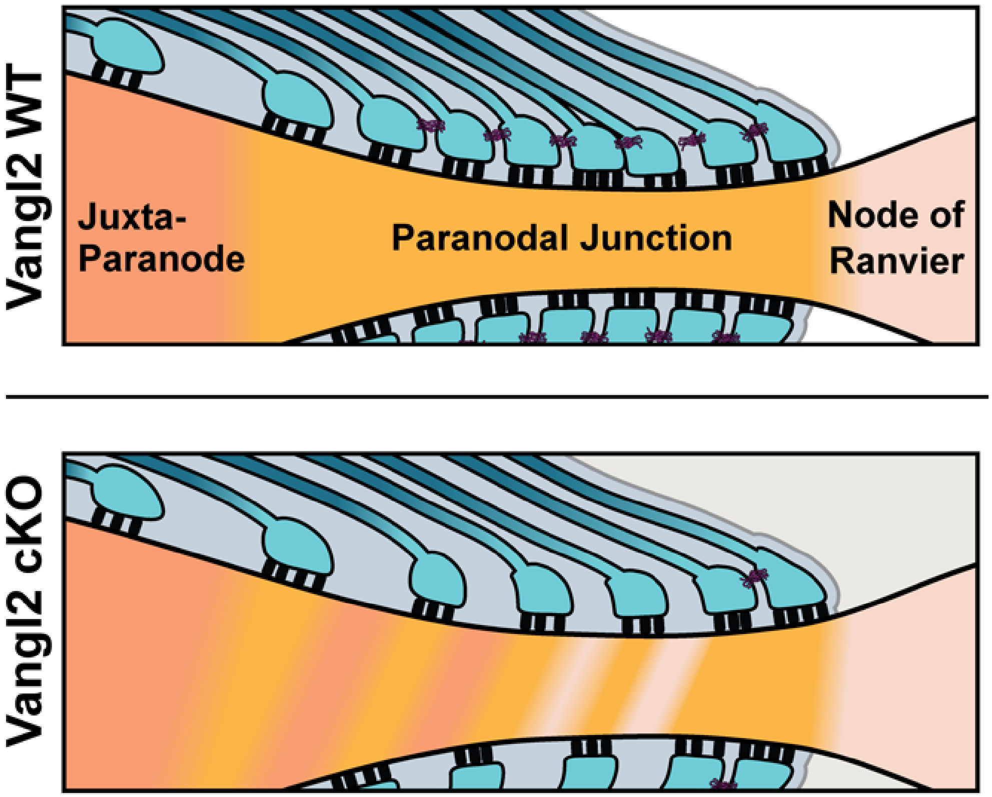

The architecture of the paranodal loops that border myelin sheaths enables rapid conduction by patterning ensheathed axons. Jarjour et al. show that the planar polarity protein Vangl2 maintains the intracellular adhesion that holds these loops together.

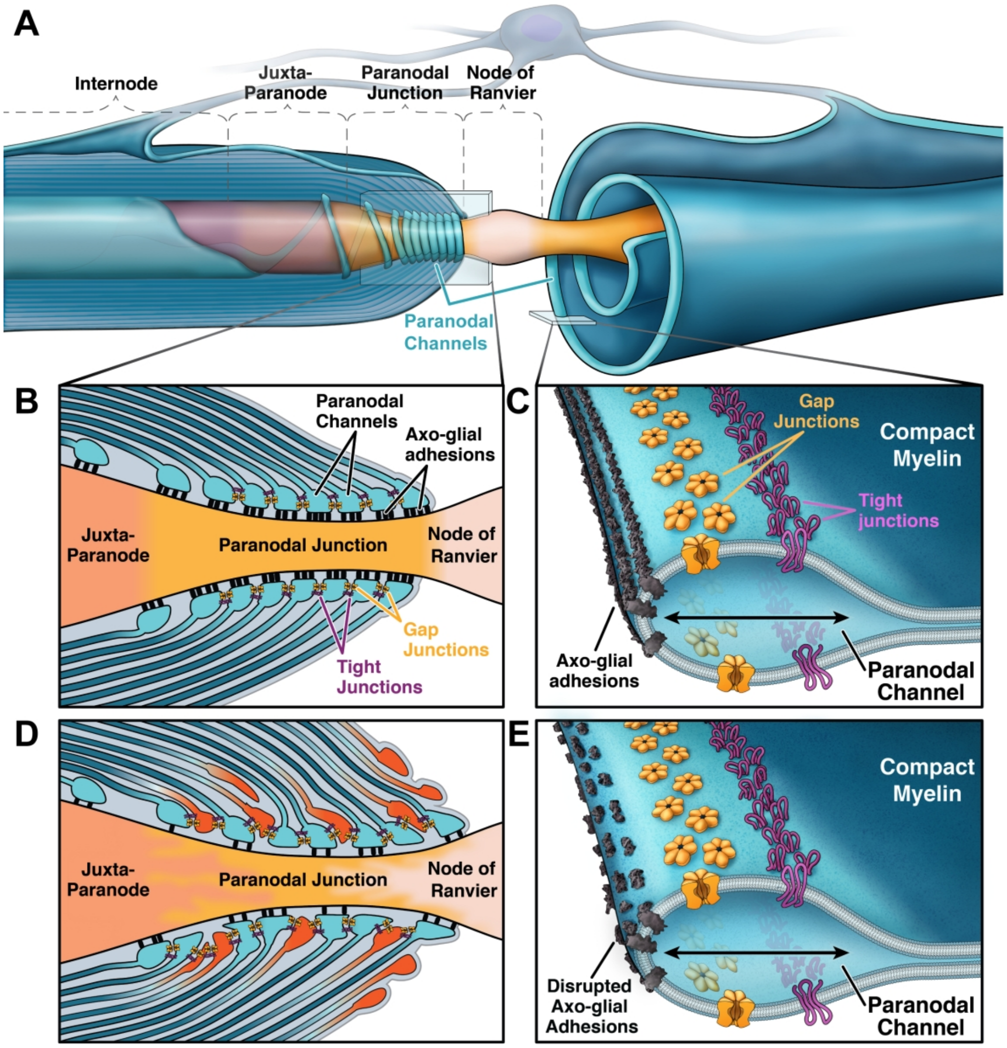

Figure 1. Organization of the CNS myelin sheath.

A: Myelin sheaths produced by oligodendrocytes consist of compacted layers of plasma membrane wrapped around the axon. The lateral edge of each sheath, which abuts the node of Ranvier (light pink) is characterized by a cytoplasm-filled channel that spirals around the paranodal axon (yellow), separating the node from the juxtaparanode (orange). The channel continues with a trajectory roughly parallel to the axon into the internodal axon (red). On the right is a partially-unfurled myelin sheath, showing the division between compact myelin (dark blue) and the cytoplasmic channel (light blue). B,C: A longitudinal cross-section of the paranode reveals that the spiral appears as a series of cytoplasm-filled loops that are adhere to both the axon and each other. The adhesions present in each paranodal loops, and the polarity of the axis along which these adhesion complexes are patterned, are shown in C. D,E: Paranodal axo-glial adhesions are disrupted in the CNS following conditional elimination of Scribble expression in oligodendroglia.

209x218mm (300 x 300 DPI)

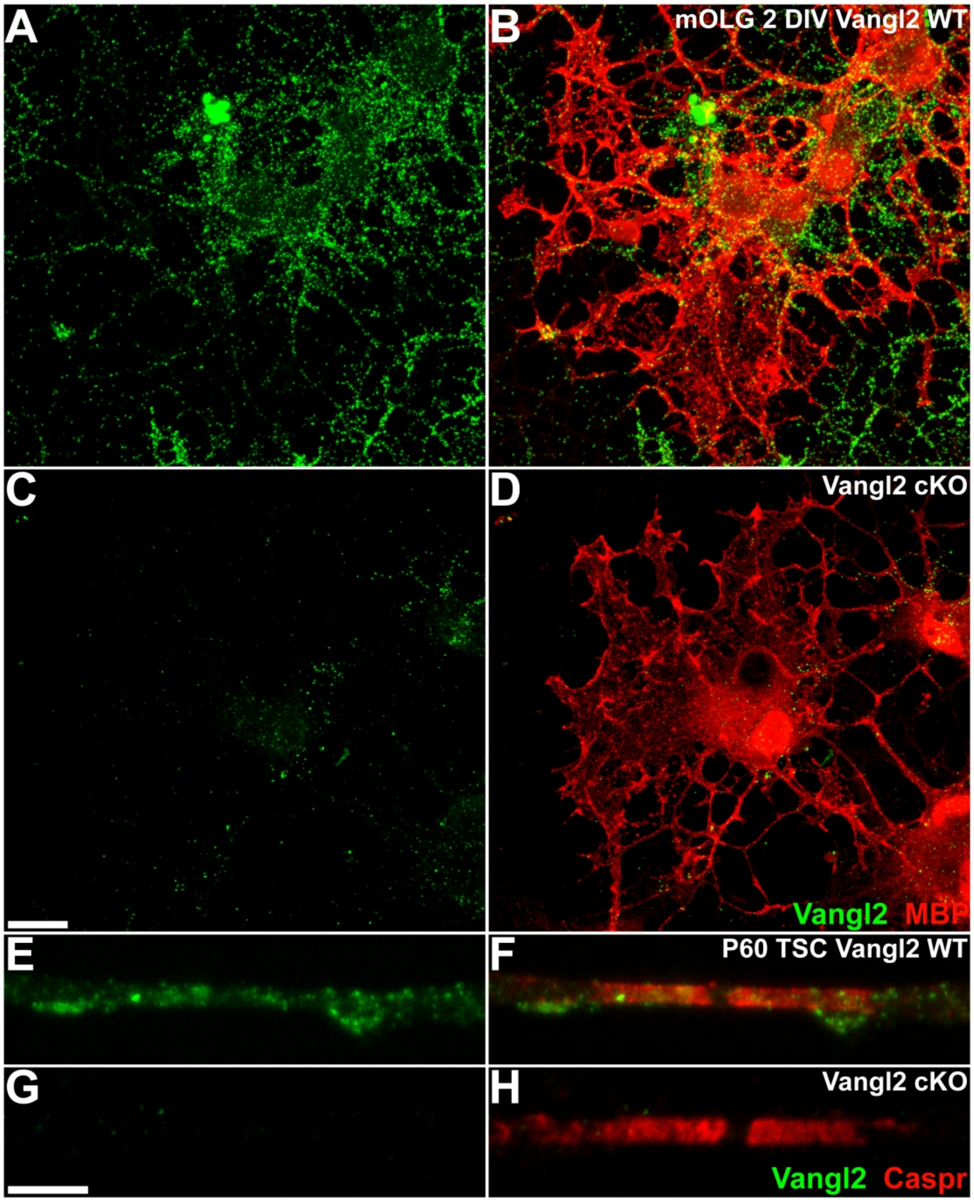

Figure 2. Elimination of Vangl2 expression in CNP-Cre:Vangl2fl/fl oligodendrocytes and paranodes.

Cultures derived from Vangl2 WT mice and differentiated for two days show expression of Vangl2 protein (A,B, green) by oligodendrocytes expressing myelin basic protein (MBP, B, red). Vangl2 protein is almost entirely absent from oligodendrocyte cultures derived from Vangl2 cKO mice (C,D). Similarly, Vangl2 protein (E,F, green) is present at paranodes labelled for Caspr (F, red) in P60 teased spinal cord fibres from Vangl2 WT mice, but not in teased fibre preparations from Vangl2 cKO mice (G,H). Scale bars: (A-D): 5 µm, (E-H): 3 µm.

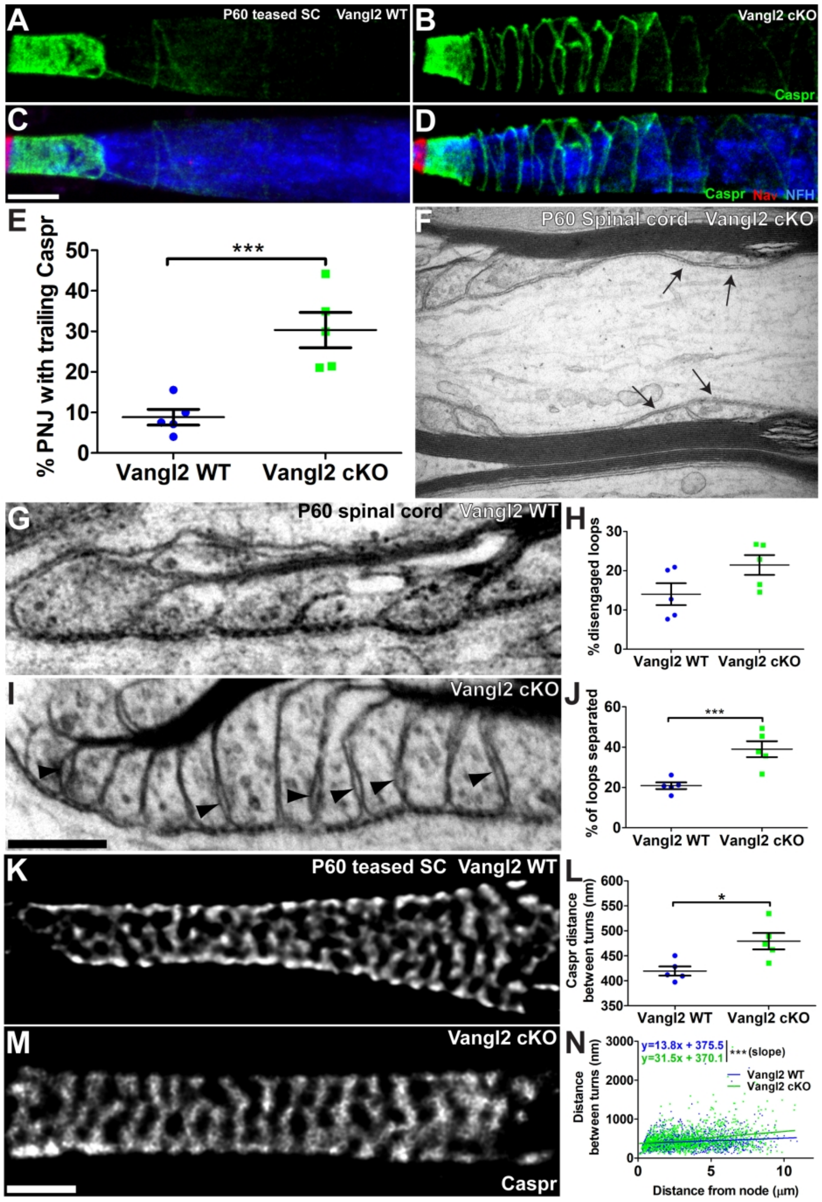

Figure 3. Disruption of the paranodal spiral in the Vangl2 conditional mutant CNS.

A-D: The paranodal spiral is disrupted in Vangl2 cKO CNS. Caspr immunolabelling (green) extends away from NaV immunolabelling (red), into the internode in Vangl2 cKO CNS (B,D), forming a looser (trailing) spiral than observed in wild-type controls (A,C). Note that the portion of the paranodal spiral closest to the node remains tightly wound, as evidenced by solid Caspr immunostaining. In panels C and D, the axon is immunolabelled for the 200 kDA neurofilament subunit (NFH, blue). The percentage of these paranodes with trailing Caspr was significantly increased (E, WT: 8.8±1.9, cKO: 30.3±4.4, p=0.0079). F: Electron microscopy reveals the presence of aberrant cytoplasm-filled myelin loops in internodal myelin in Vangl2 cKO spinal cord at P60 (F, arrows). G-J: Paranodal loops largely remain adhered to the axonal surface in the Vangl2 cKO CNS (I), as in wild-type CNS (G, quantification in H, Percentage of paranodal loops disengaged from the axonal surface: WT: 14.0±2.8, cKO: 21.6±2.4, p=0.0952). An increase in the percentage of paranodal loops that were separated from each other was observed in Vangl2 cKO spinal cord (I, arrowheads), relative to wild-type (G, quantification in J, Percentage of interfaces between neighbouring paranodal loops showing separation: WT: 20.9±1.6, cKO: 39.0±4.0, p=0.0079). K-N: Superresolution gSTED confocal imaging of the Caspr spiral further revealed that spacing between turns of the paranodal spiral is increased in Vangl2 cKO teased spinal cord fibres at P60 (M) relative to wild-type paranodes (K, quantification in L,N; Mean distance between turns of the paranodal spiral: WT: 419.5±9.2 nm, cKO: 479.2±16.4 nm, p = 0.016 ; Equation of best-fit line: WT: $y=13.8\pm2.5x + 375.5\pm10.0$, cKO: $y=31.5\pm3.1x + 370.1\pm13.4$, $p < 0.0001$ (slope)). All data are represented as mean ± SEM. n = 5 mice per genotype. Statistical analyses were performed using the Mann-Whitney test. A-E: At least 40 paranodes were analysed per animal. G-K, K-N: At least 20 paranodes were analysed per animal. Scale bars (A-D): 5 µm, (G,I): 250 nm, (K,M): 1 µm.

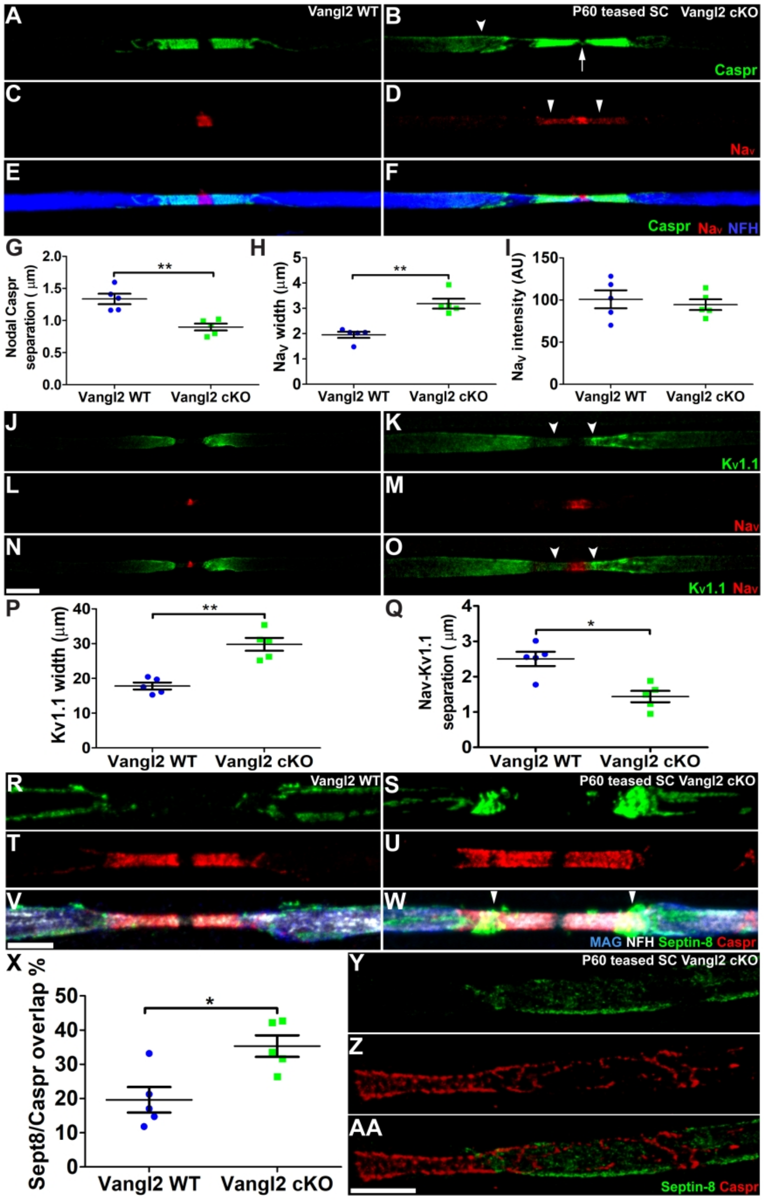

Figure 4. Oligodendroglial Vangl2 expression is required for domain organization of myelinated CNS axons at nodes of Ranvier.

In wild-type CNS, Caspr-immunopositive paranodes (green) flank NaV-immunopositive nodes of Ranvier (red), with a clear separation existing between neighbouring paranodes (A,C,E). In Vangl2 cKO CNS (B,D,F) the Caspr domain extends both into the internode (B, arrowhead) and into the node of Ranvier (B, arrow). This shortens the node (quantified in G, distance between paranodal Caspr immunolabelling across node of Ranvier (μm): WT: 1.34±0.08, cKO: 0.90±0.05, p=0.0079). The nodal NaV-immunolabelled domain is widened and spreads laterally into the paranodes (D, arrowheads, quantified in H; width of nodal NaV immunolabelling (μm): WT: 1.9±0.1, cKO: 3.2±0.2, p=0.0079). No significant change in nodal sodium channel immunolabelling intensity was observed in Vangl2 cKO CNS (I; WT: 100.8±10.6, cKO: 94.4±6.4, p = 0.8413). In wild-type CNS, a clear paranodal separation is observed between nodal NaV (red) and juxtaparanodal KV (green) immunolabeling (J,L,N). In Vangl2 cKO (K,M,O), the KV-immunolabeled area is widened (P; width of KV1.1 immunolabelling (μm): WT: 17.8±1.0, cKO: 28.9±3.2, p=0.0079) and invades the paranodal domain (K, O, arrowheads), with the distance between NaV and KV1.1 immunolabelling reduced (Q; WT: 2.5±0.2μm, cKO: 1.5±0.2μm, p=0.0159). (Q-AA): Septin-8 is mislocalized to paranodes in Vangl2 cKO P60 teased spinal cord fibres. Septin-8 (green), which is restricted to the internodal inner tongue in wild-type fibres (R,T,V), extends into Caspr-immunopositive (red) paranodal regions in Vangl2 cKO fibres (S,U,W, arrowheads), with the percentage length of the Caspr-immunopositive domain that overlapped with Septin-8 labelling being significantly increased (X; WT: 19.6±3.7, cKO: 35.3±3.1, p=0.0317). Myelin was immunolabelled for MAG (blue) and axons for NFH (white). Superresolution imaging using gated STED reveals that Septin-8 (green, Y,AA) and Caspr (red, Z,AA) do not co-localise at paranodes. All data are represented as mean ± SEM. n = 5 mice per genotype. Statistical analyses were performed using the Mann-Whitney test. A-H: At least 20 nodes of Ranvier were analysed per animal. I-P: At least 40 paranodes were analysed per animal. Scale bars: (A-F and J-O): 5 μm, (Y-AA): 300 nm.

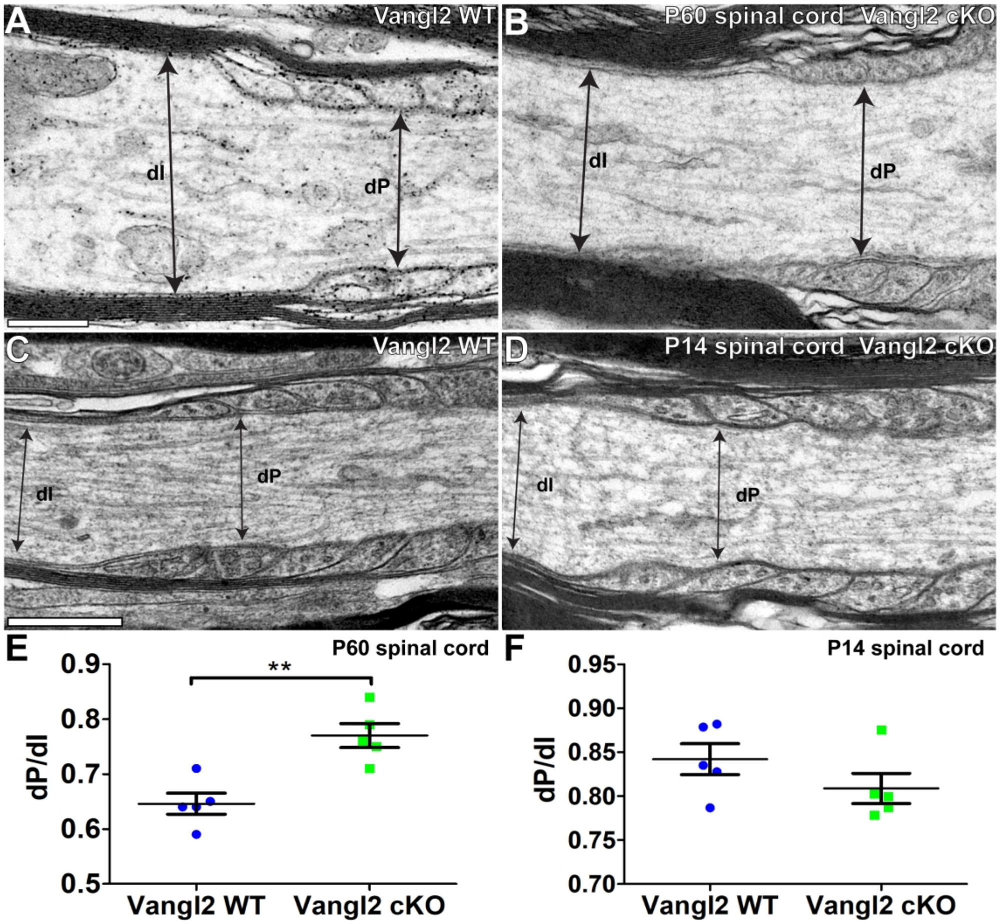

Figure 5. Vangl2 is required for local regulation of axon diameter in myelinated CNS axons.

In wild-type spinal cord at P60 (A), paranodal axon diameter (dP) is smaller than internodal diameter (dI). A relative increase in dP is observed in Vangl2 cKO spinal cord at P60 (B), resulting in an increased dP/dI ratio relative to that observed in wild-type controls (E; WT: 0.73±0.02, cKO: 0.77±0.02, p=0.0157). dP/dI ratio is not significantly different between Vangl2 WT and cKO in P14 spinal cord (C,D,F; WT: 0.84±0.02, cKO: 0.81±0.02, p=0.2222). All data are represented as mean ± SEM. n = 5 mice per genotype. Statistical analyses were performed using the Mann-Whitney test. At least 25 paranodes were analysed per animal, per time point. Scale bars: (A,B) and (C,D): 500 nm.

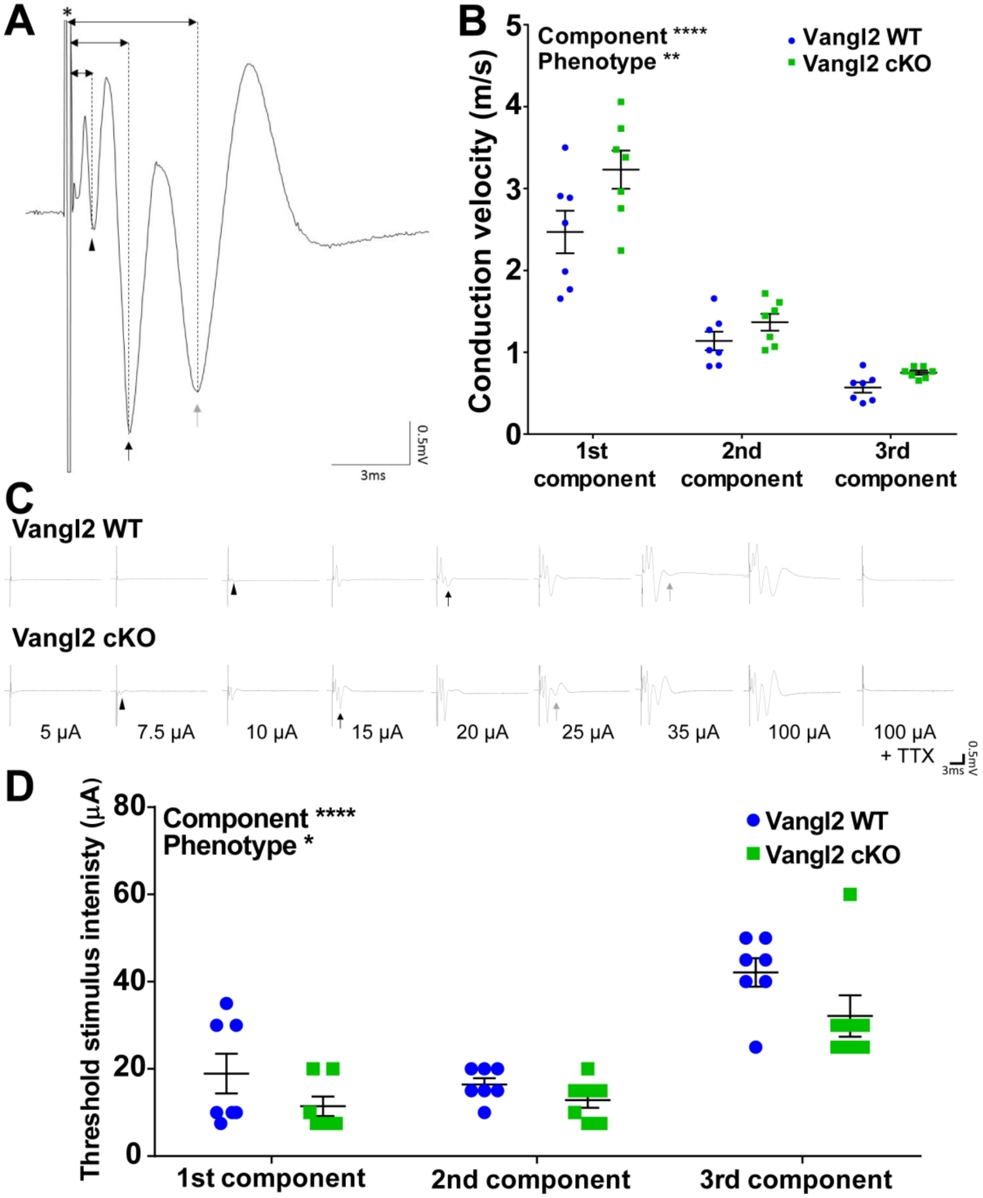

Figure 6. Loss of Vangl2 expression by oligodendrocytes increases the conductivity of myelinated CNS axons.

A representative compound action potential (CAP) recording showing three peaks is shown in (A). The first component is labelled with a black arrowhead, the second with a black arrow, and the third with a grey arrow. The double-headed arrows represent latency, which is measured as the time between the stimulus artefact (asterisk) and the negative peak of each triphasic component. The mean conduction velocity of the three CAP peaks is increased in Vangl2 cKO optic nerve (B; 1st component: WT: 2.47±0.26 m/s, cKO: 3.23±0.23; 2nd component: WT: 1.14±0.11, cKO: 1.37±0.10; 3rd component: WT: 0.57±0.06, cKO: 0.75±0.03, $p = 0.0047$). The mean minimum stimulus intensity at which each component of the CAP was first detected was decreased in Vangl2 cKO optic nerve, as shown by representative traces (C, quantification in D; 1st component: WT: 18.9±4.6 μA, cKO: 11.4±2.2; 2nd component: WT: 16.4±1.4, cKO: 12.9±1.8; 3rd component: WT: 42.1±3.2, cKO: 32.1±4.7, $p = 0.0123$). Statistical analyses were performed using two-way ANOVA followed by Sidak's multiple comparisons test (B,D). N = 7 nerves from four animals per genotype.

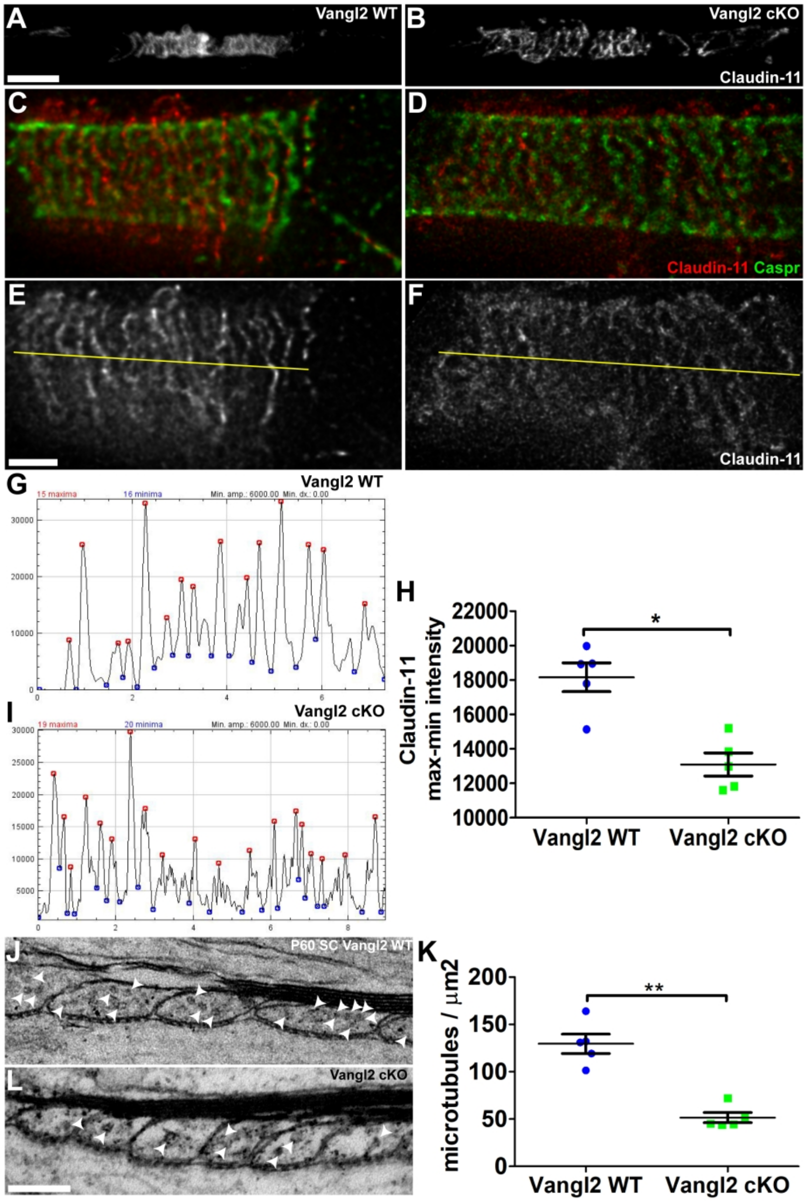

Figure 7. Vangl2 controls the distribution of the autotypic tight junction protein Claudin-11 within CNS paranodal myelin.

(A-I): Standard and superresolution gated stimulation emission depletion (gSTED) confocal microscopy revealed altered distribution of Claudin-11 in P60 Vangl2 cKO spinal cord paranodes. The spiral of paranodal oligodendroglial Claudin-11 immunolabelling is loosened and elongated laterally along the axon in teased spinal cord preparations from Vangl2 cKO mice (B) relative to those from Vangl2 WT (A). In Vangl2 cKO paranodes (D,F), the intensity of Claudin-11 distribution (red in C,D, white in E,F) appeared diffuse relative to that observed in wild-type paranodes (C,E). Caspr-immunolabelled axo-glial adhesions are shown in green (C,D). When Claudin-11 immunolabelling intensity is plotted across individual paranodes (along the yellow lines in E and F), analysis of intensity maxima (red dots in G,I and minima (blue dots in G,I) revealed that the difference between maxima and minima was decreased at Vangl2 cKO paranodes (H). (J-L): Microtubule density is reduced in the Vangl2 cKO paranodal spiral. In P60 Vangl2 cKO spinal cord (L), the density of microtubules (white arrowheads) within paranodal loops was decreased relative to that observed in wild-type animals (J, quantification in K; WT: 129.5±10.2 microtubules/μm2, cKO: 51.6±5.4 microtubules/μm2, p=0.0079). All data are represented as mean ± SEM. n = 5 mice per genotype. (C-I): At least 20 paranodes were analysed per animal. (J-L): At least 50 paranodal loops from at least 10 paranodes were analysed per animal. Statistical analyses were performed using the Mann-Whitney test. Scale bars: (A,B): 5 μm ,(C-F): 1 μm, (J,L): 200 nm.

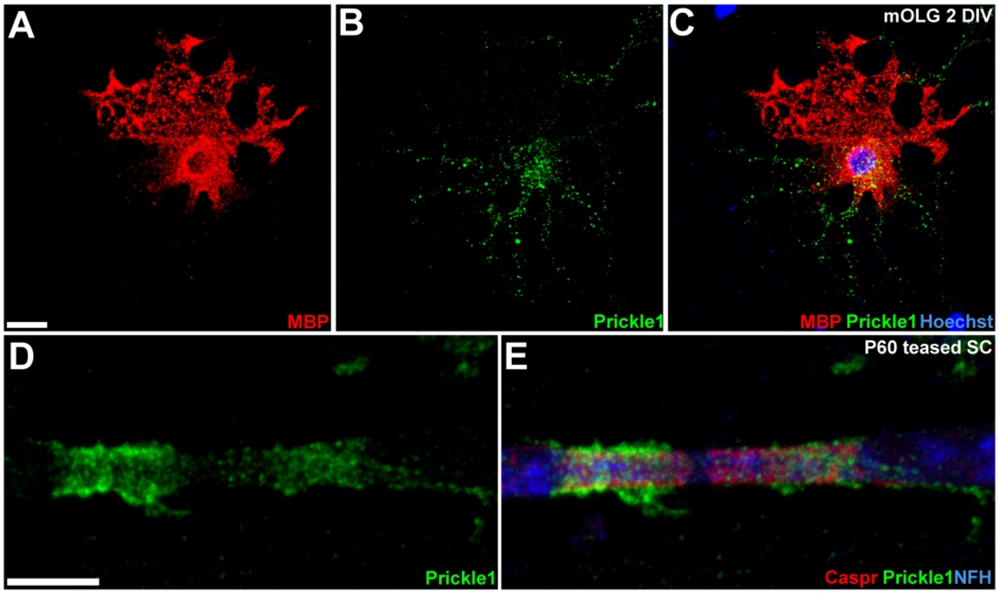
A
MBP
B
Prickle1
C
mOLG 2 DIV
MBP Prickle1 Hoechst
D
Prickle1
E
P60 teased SC
Caspr Prickle1 NFH

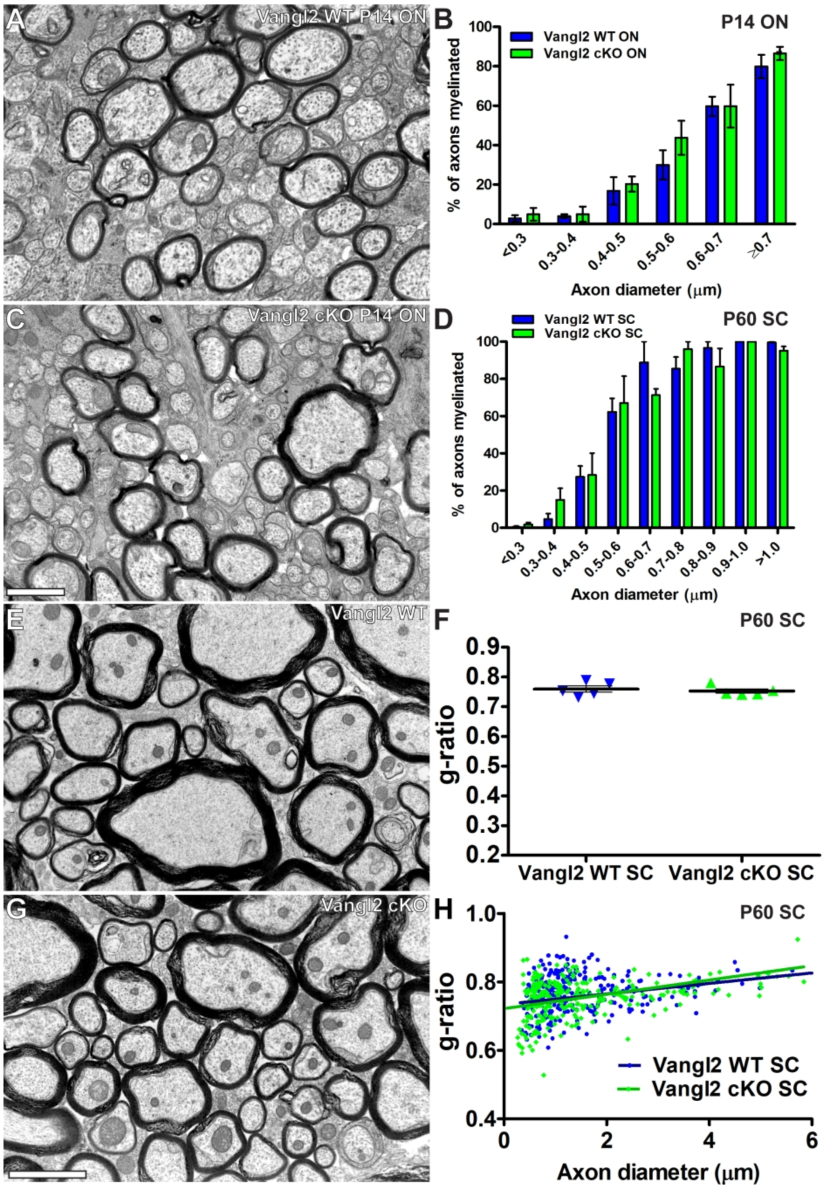
A
Vangl2 WT P14 ON
B
P14 ON
Vangl2 WT ON
Vangl2 cKO ON
% of axons myelinated
100
80
60
40
20
0
<0.3
0.3-0.4
0.4-0.5
0.5-0.6
0.6-0.7
≥0.7
Axon diameter (μm)
C
Vangl2 cKO P14 ON
D
Vangl2 WT SC
Vangl2 cKO SC
P60 SC
% of axons myelinated
<0.3
0.3-0.4
0.4-0.5
0.5-0.6
0.6-0.7
0.7-0.8
0.8-0.9
0.9-1.0
>1.0
Axon diameter (μm)
E
Vangl2 WT
F
P60 SC
g-ratio
0.9
0.8
0.7
0.6
0.5
0.4
0.3
0.2
Vangl2 WT SC
Vangl2 cKO SC
G
Vangl2 cKO
H
P60 SC
g-ratio
1.0
0.8
0.6
0.4
0
2
4
6
Vangl2 WT SC
Vangl2 cKO SC
Axon diameter (μm)

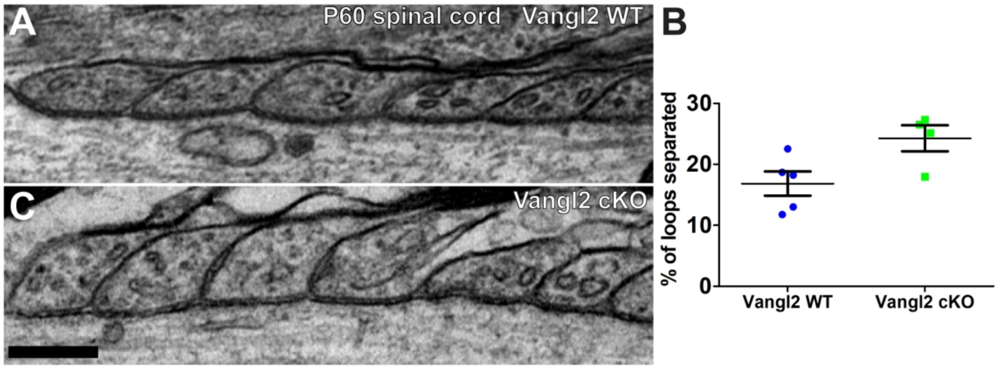
A
P60 spinal cord
Vangl2 WT
B
C
Vangl2 cKO
% of loops separated
30
20
10
0
Vangl2 WT
Vangl2 cKO

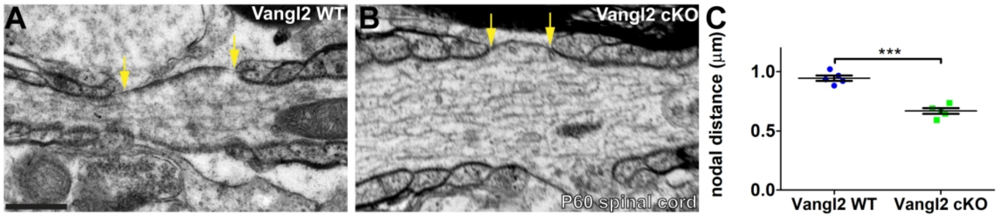
A
Vangl2 WT
B
Vangl2 cKO
P60 spinal cord
C
nodal distance (μm)
1.0
0.5
0.0
***
Vangl2 WT
Vangl2 cKO

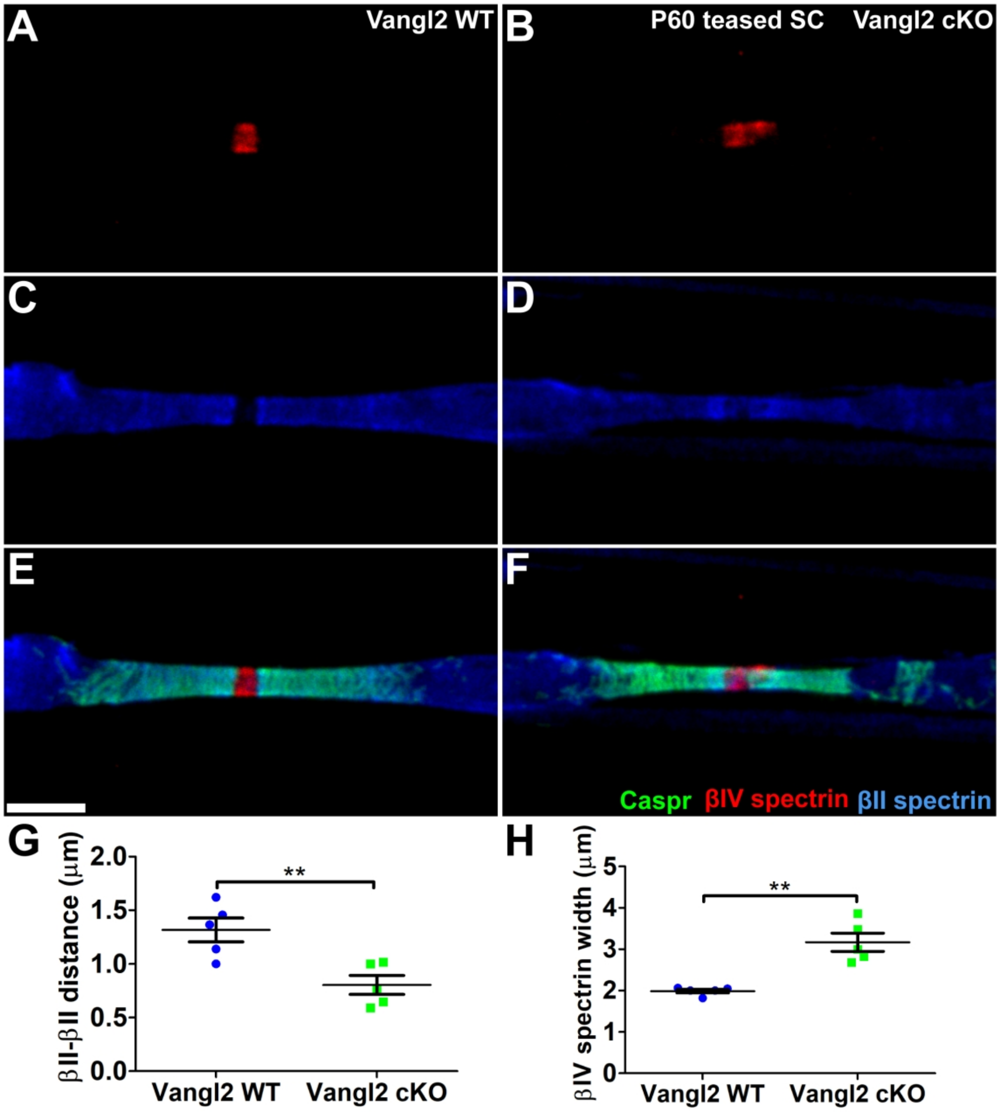
A
Vangl2 WT
B
P60 teased SC
Vangl2 cKO
C
D
E
F
Caspr βIV spectrin βII spectrin
G
βII-βII distance (μm)
2.0
1.5
1.0
0.5
0.0
**
Vangl2 WT
Vangl2 cKO
H
βIV spectrin width (μm)
5
4
3
2
1
0
**
Vangl2 WT
Vangl2 cKO

SUPPORTING INFORMATION

Supplemental Figure 1. Prickle1 is expressed by oligodendrocytes and is concentrated at CNS paranodes.

A-C: Prickle1 (green) is localised to the cell body and processes of cultured mouse oligodendrocytes labelled with antibodies against myelin basic protein (MBP, red) at 2 days *in vitro* (DIV), but is excluded from myelin-like sheets. Nuclei were labelled with Hoechst dye (blue). D,E: Prickle1 (green) is concentrated at paranodes in P60 spinal cord. In panel E, the axon is immunolabelled for the 200 kDA neurofilament subunit (NFH, blue). The distribution of Prickle1 overlaps with the paranodal marker Caspr (red). Scale bars (A-C): 10 µm, (D,E) 5 µm.

Supplemental Figure 2. Vangl2 does not regulate myelin initiation or thickness

(A-D): Myelin initiation occurs normally in Vangl2 cKO CNS. In P14 optic nerve, no differences were observed in the proportion of axons that were myelinated in Vangl2 cKO (C), relative to wild-type (A). This was true for all axon diameters (B). This remained true in adult mice, as no differences in the proportion of myelinated axons were observed in P60 spinal cord (D). Percentage of axons myelinated in P14 optic nerve: < 0.3 μm: WT: 2.9±1.6, cKO: 5.0±3.2, 0.3-0.4 μm: WT: 4.0±1.0, cKO: 5.0±3.9, 0.4-0.5 μm: WT: 16.8±7.0, cKO: 20.3±3.8, 0.5-0.6 μm: WT: 30.0±7.5, cKO: 43.8±8.7, 0.6-0.7 μm: WT: 59.7±4.9, cKO: 59.8±10.8, > 0.7 μm: WT: 79.9±5.9, cKO: 86.5±3.4. Percentage of axons myelinated in P60 ventral spinal cord: < 0.3 μm: WT: 0.5±0.5, cKO: 1.9±1.0, 0.3-0.4 μm: WT: 4.7±2.9, cKO: 15.0±6.2, 0.4-0.5 μm: WT: 27.3±5.9, cKO: 28.4±11.7, 0.5-0.6 μm: WT: 62.3±7.3, cKO: 67.1±14.3, 0.6-0.7 μm: WT: 88.9±11.1, cKO: 71.3±3.3, 0.7-0.8 μm: WT: 85.5±6.3 , cKO: 96.0±4.0, 0.8-0.9 μm: WT: 96.7±3.3, cKO: 86. 7±9.7, 0.9-1.0 μm: WT: 100±0, cKO: 100±0, > 1.0 μm: WT: 99.6±0.4, cKO: 95.2±2.3. $p > 0.05$ for all comparisons. n = 6 animals for P14 WT and n = 5 animals for P14 cKO, P60 WT, P60 cKO. At least 100 axons were analysed per animal, per time point. Statistical analyses were performed using two-way ANOVA with Bonferroni post-tests. (E-H): No differences in myelin thickness were observed in the Vangl2 cKO CNS. In P60 spinal cord, myelin thickness appeared similar in Vangl2 cKO (G) and wild-type (E) tissue. No differences in g-ratio were observed in the absence of oligodendroglial Vangl2 expression (F,H). Mean g-ratio: WT: 0.759 ± 0.011, cKO: 0.753 ± 0.007, $p = 0.8413$ (Mann-Whitney test). Best-fit lines obtained through linear regression analysis when plotting axon diameter vs. g-ratio: WT slope: 0.0153 ± 0.0049, cKO slope: 0.0209 ± 0.0056, $p = 0.4547$. WT y-intercept: 0.735 ± 0.009, cKO y-intercept: 0.722 ± 0.010, $p = 0.618$. n = 5 animals per genotype, at least 50 myelinated axons analyzed per animal. Scale bars (A,C): 1 μm, (E,G): 2 μm.

Supplemental Figure 3. Separation between paranodal loops in the developing Vangl2 cKO CNS.

At postnatal day 14, a non-statistically significant increase in the percentage of paranodal loops that were separated from each other was observed in Vangl2 cKO spinal cord (C), relative to wild-type (A, quantification in B, Percentage of interfaces between neighbouring paranodal loops showing separation: WT: 16.8±2.0, cKO: 24.3±2.1, p=0.11). All data are represented as mean ± SEM. n = 5 mice for WT, n= 4 mice for cKO. Statistical analyses were performed using the Mann-Whitney test. At least 10 paranodes were analysed per animal. Scale bar: 200 nm.

Supplemental Figure 4. The node of Ranvier is shortened in Vangl2 cKO CNS.

The length of the node of Ranvier is decreased in Vangl2 cKO P60 spinal cord (B) relative to that observed at wild-type nodes (A, quantified in C; distance across node of Ranvier (µm): WT: 0.94±0.02, cKO: 0.67±0.02, p = 0.0079). All data are represented as mean ± SEM. n = 5 mice per genotype. Statistical analyses were performed using the Mann-Whitney test. At least 20 nodes of Ranvier were analysed per animal. Scale bar: 500 nm.

Supplemental Figure 5. The axonal spectrin cytoskeleton is disrupted in Vangl2 cKO CNS.

Axonal patterning defects at the node-paranode boundary in Vangl2 cKO CNS results in the disruption of the underlying spectrin cytoskeleton. In wild-type CNS, βII spectin labelling (C,E, blue) is excluded from βIV spectrin-immunopositive nodes of Ranvier (A,E, red), as is Caspr-immunopositive paranodal labelling (E, green). In Vangl2 cKO CNS, the βIV spectrin domain, like the Na_V domain, widens (B,F,H), while the βII spectin domain (D,F), like the Caspr domain (F), extends into the node of Ranvier, resulting in the gap between βII spectin domains being decreased (G). Width of nodal βIV spectrin immunolabelling (µm): WT: 1.98±0.04, cKO: 3.2±0.2, p = 0.0079. Distance between βII spectin immunolabelling across node of Ranvier (µm): WT: 1.37±0.08, cKO: 0.78±0.08, p = 0.0278. All data are represented as mean ± SEM. n = 5 mice per genotype. Statistical analyses were performed using the Mann-Whitney test. At least 20 nodes of Ranvier were analysed per animal. Scale bar: 5 µm.